Acta Pharmaceutica Sinica B 2025;15(9):4730−4750

Chinese Pharmaceutical Association
Institute of Materia Medica, Chinese Academy of Medical Sciences

Acta Pharmaceutica Sinica B

www.elsevier.com/locate/apsb
www.sciencedirect.com

ORIGINAL ARTICLE

Astrocyte FGF7/FGFR2 autocrine signaling mediates neuroinflammation and promotes MPTP-induced degeneration of dopaminergic neurons

Xin Sun[a,†], Yueping Wang[a,†], Yajie Zhang[a], Ruixue Han[a], Min Wang[a], Jing Zhang[a], Ting Sun[b], Yang Liu[b], Gang Hu[a,*], Lei Cao[a,c,*], Ming Lu[a,c,*]

[a]*Jiangsu Key Laboratory of Neurodegeneration, Department of Pharmacology, Nanjing Medical University, Nanjing 211166, China*
[b]*Department of Pharmacology, School of Medicine and Holistic Integrative Medicine, Nanjing University of Chinese Medicine, Nanjing 210023, China*
[c]*Changzhou Second People's Hospital, Changzhou Medical Center, Nanjing Medical University, Changzhou 213000, China*

Received 22 November 2024; received in revised form 29 March 2025; accepted 8 May 2025

KEY WORDS

β-Arrestin2;
FGF7/FGFR2 autocrine signaling;
Neuroinflammation;
Reactive astrocytes;
Dopaminergic neurons;
Parkinson's disease;
Neuroprotection;
G protein-coupled receptors

Abstract Reactive astrocytes, which exhibit a correlation with the degeneration of dopaminergic neurons, are present in a considerable number during the progression of Parkinson's disease (PD). However, the underlying factors shaping astrocyte reactivity and neuroinflammation in PD remain inadequately elucidated. Here, we demonstrate that fibroblast growth factor 7 (FGF7)/FGF receptor 2 (FGFR2) autocrine signaling intensifies astrocyte reactivity and inflammation. Genetic deletion of *Arrb2*, *β*-Arrestin2 encoding gene, led to escalated astrocyte reactivity in MPTP-treated mice, which was further substantiated in astrocyte-specific *Arrb2* knockdown mice. RNA sequencing profiling of *Arrb2* knockout astrocytes identified *Fgf7* as a critical effector of astrocyte reactivity. Subsequently, conditional knockdown of *Fgf7* and its receptor *Fgfr2* in astrocytes elicited advantageous effects for MPTP-treated mice by restraining the inflammatory phenotypic transition of reactive astrocytes. Furthermore, deletion of astrocytic *Fgf7* mitigated MPTP-induced pathology in *Arrb2* knockout mice. Mechanistically, STAT1 was distinguished as the transcription factor suppressing *Fgf7* expression, while *β*-Arrestin2 counteracted

*Corresponding authors.
E-mail addresses: lum@njmu.edu.cn (Ming Lu), leicao@njmu.edu.cn (Lei Cao), ghu@njmu.edu.cn (Gang Hu).
[†]These authors made equal contributions to this work.

Peer review under the responsibility of Chinese Pharmaceutical Association and Institute of Materia Medica, Chinese Academy of Medical Sciences.

https://doi.org/10.1016/j.apsb.2025.07.012

the proteasomal degradation of STAT1 by binding to RNF220, an E3 ubiquitin ligase for STAT1. More importantly, selectively engaging dopamine D2 receptor (Drd2)/β-Arrestin2-biased signaling using the agonist UNC9995 exhibited therapeutic potential in MPTP-treated mice *via* moderation of astrocytic FGF7 production, thereby restoring balance in astrocyte reactivity. Collectively, our study bridges a crucial knowledge gap by elucidating the novel functions of FGF family members within the central nervous system, particularly within the context of PD. The autocrine signaling of FGF7/FGFR2 represents a novel mechanism and a potential druggable target for modulating astrocyte-derived inflammation.

1. Introduction

Parkinson's disease (PD) is a neurodegenerative disease featured by the loss of dopaminergic (DA) neurons and the accumulation of α-synuclein in the substantia nigra pars compacta (SNpc)[1]. Although dopamine replacement/agonist therapy is currently available to manage PD motor symptoms, it does not affect disease progression[2,3]. As a result, numerous disease-modifying therapies based on pathophysiological findings have been investigated in preclinical experiments and clinical trials, but all have failed in clinical translation[4]. These clinical failures emphasize the need to further explore the complex pathogenesis of PD.

Astrocytes are one of the most abundant cells throughout the adult central nervous system and have been observed to exhibit a dramatic increase in reactivity in the context of PD. Previously, reactive astrocytes were divided into neurotoxic A1 and neuroprotective A2 phenotypes identified by correlative signatures of certain genes[5]. However, recent studies subdivided the phenotypes of reactive astrocytes into subpopulations defined by different gene expressions[6,7]. Studies utilizing advanced transcriptomic technologies, such as single-cell and single-nuclei RNA sequencing have delineated the distinct subtypes and functional states of reactive astrocytes across various pathological contexts, and have identified disease-specific astrocyte signatures and underscored the importance of comprehensive functional characterization to understand the complex and heterogeneous nature of astrocyte reactivity in health and disease[8-10]. For instance, apolipoprotein E and CD49f have been implicated in the formation and identification of distinct reactive astrocyte populations, further emphasizing the need for a multifaceted approach to dissect the diversity and functional roles of astrocytes in the context of neurological disorders[11,12]. In PD, reactive astrocytes trigger a potent pro-inflammatory reaction, thereby contributing to the disease progression[13,14]. Consequently, abrogating detrimental actions of reactive astrocytes may become a promising strategy for PD treatment. However, molecular mechanisms underscoring the phenotypic transformation of reactive astrocytes in PD progression are poorly documented.

Growing evidence suggests that the fibroblast growth factor (FGF) family exerts significant influence on the preservation of both peripheral and central nervous system homeostasis. This is achieved through the regulation of fundamental physiological processes, such as cellular proliferation and differentiation. Moreover, FGFs are implicated in pathological processes, including inflammation and cell death[15,16]. For instance, FGF7 is expressed both in the cytosol and nucleoplasm, with the capacity for secretion into extracellular spaces to modulate downstream signaling cascades *via* autocrine and paracrine modes of action[17,18]. While elevated FGF7 expression has been documented in PD, Alzheimer's disease, and amyotrophic lateral sclerosis[19-21], its precise role in the central nervous system and in neurological diseases remains poorly understood. In PD, emerging evidence highlights the involvement of FGF family members, including FGF1, FGF2, and FGF9 in neuroprotective mechanisms targeting DA neurons[17]. The FGF signaling cascade has also been identified as a critical factor in orchestrating the intricate morphology of reactive astrocytes[22]. As a consequence, exploring the operative mechanism by which FGF signaling modulates astrocyte reactivity holds promise in identifying potential therapeutic targets for PD.

β-Arrestins were initially identified as components involved in G protein-coupled receptors (GPCRs) desensitization[23], while accumulating evidence has demonstrated that β-Arrestins are crucial signal transducers and scaffolds mediating intracellular events beyond the canonical internalization of GPCRs[24-26]. As a prototypical GPCR, dopamine D2 receptor (Drd2) exerts its canonical signaling effects *via* Gαi protein-coupled mechanisms, engaging classical G protein-dependent pathways. Beyond this traditional modality, Drd2 facilitates the recruitment of β-Arrestins to the plasma membrane, thereby initiating β-Arrestin-mediated non-canonical signaling cascades. These divergent pathways are classified under the paradigm of biased signaling, specifically recognized as Drd2/β-Arrestins-biased signaling mechanisms[27]. Previously, we and other groups highlighted the beneficial effects of β-Arrestin2 on PD progression by inhibiting neuroinflammation[28-30]. Specifically, we observed that global knockout of *Arrb2*, the β-Arrestin2 encoding gene, did not result in significant loss of DA neurons at baseline. However, it did lead to an increase in astrocyte reactivity. Interestingly, mice lacking *Arrb2* exhibited heightened susceptibility to 1-methyl-4-pheny L-1,2,3,6-tetrahydropyridine (MPTP)-induced damage to DA neurons, thereby exacerbating the progression of PD[28]. This phenomenon suggests that the beneficial effects of β-Arrestin2 on PD progression may be attributed to its regulation of astrocyte reactivity. To this end, we hypothesize that β-Arrestin2 functions as a negative regulator of astrocyte reactivity, providing neuroprotection by maintaining the phenotype of astrocytes during the progression of PD.

In this study, RNA sequencing was performed in astrocytes lacking *Arrb2* to explore the regulatory role of β-Arrestin2 in astrocyte reactivity. *Arrb2* deletion elevates FGF7 production thereby activating the FGF7/FGFR2 signaling to convert astrocytes into reactive phenotype. Mechanistically, β-Arrestin2 directly binds to RING Finger Protein 220 (RNF220), an E3 ubiquitin ligase, to inhibit the ubiquitination and proteasomal degradation of signal transducer and activator of transcription 1 (STAT1), which is a negative regulator of *Fgf7* transcription. To validate the potential role of β-Arrestin2 in modulating astrocyte phenotype in the

progression of DA neuronal death, we administered UNC9995, a Drd2/β-Arrestin2-biased agonist, to MPTP-treated mice. Remarkably, we observed that UNC9995 treatment decelerated the progression of DA neuronal death by impeding the FGF7-induced neurotoxic astrocyte reactivity. Together, this work demonstrates that β-Arrestin2 hinders FGF7-dependent neurotoxic astrocyte reactivity, highlighting promising molecular targets for the development of astrocyte-based disease-modifying therapies for PD.

2. Materials and methods

2.1. Animals

C57BL/6J mice (3 months old) were procured from the animal center of Nanjing Medical University. We purchased β-Arrestin1 knockout (*Arrb1* KO) mice from Jackson Laboratory, and β-Arrestin2 knockout (*Arrb2* KO) mice from Gang Pei's laboratory (Tongji University, China). All mice were bred and housed at the animal center of Nanjing Medical University, with *ad libitum* access to food and water at 22 ± 2 °C and a 12/12 h-light/dark cycle. Animal experiments were approved by Institutional Animal Care and Use Committee of the Nanjing Medical University (IACUC No. 1601153-3).

2.2. The MPTP mouse model

Male C57BL/6J mice (3 months old) and *Arrb2* KO mice (3 months old) were utilized to establish the subacute PD model by administration of MPTP, as previously described[14]. Briefly, mice were injected with MPTP (20 mg/kg, s.c.) once daily for 5 consecutive days, followed by a 7-day resting period. To achieve astrocytic knockdown of *Arrb2*, *Ffg7*, and *Fgfr2*, relative AAV2/9 were injected into the Substantia nigra region of the mice. The MPTP model was induced 3 weeks following the virus injection. For the UNC9995 treatment, mice were administered with UNC9995 (2 mg/kg, i.p., daily) for 11 days, ranging from 3 days before to 3 days after the MPTP model was induced. Behavioral tests were conducted 7 days after the MPTP model or UNC9995 treatment.

2.3. The LPS mouse model

Male C57BL/6J mice (3 months old) were injected with LPS (2.5 μg/μL, 1 μL) bilaterally into the substantia nigra. The injection coordinates were as follows: A/P −3.0 mm, R/L ±1.3 mm, and D/V −4.5 mm. The model was established one week after LPS injection. For the UNC9995 treatment, mice were administered with UNC9995 (2 mg/kg, i.p., daily) for 13 days, ranging from 3 days before to 3 days after the LPS model was induced.

2.4. FGF7 injection

Male C57BL/6J mice (3 months old) were injected with FGF7 (2.5 μg/μL, 1 μL) bilaterally into the substantia nigra. The injection coordinates were as follows: A/P −3.0 mm, R/L ±1.3 mm, and D/V −4.5 mm. Samples were collected on Days 3 and 7 after FGF7 injection.

2.5. Adeno-associated virus (AAV) injection

The adeno-associated viruses expressing mouse *Arrb2* siRNA (HBAAV2/9-*Gfap*-mir30-*m-Arrb2-Egfp*) or mouse *Fgf7* siRNA (HBAAV2/9-*Gfap*-mir30-*m-Fgf7-Egfp*) or mouse *Fgfr2* siRNA (HBAAV2/9-*Gfap*-mir30-*m-Fgfr2-Egfp*) or control siRNA (HBAAV2/9-*Gfap-Egfp*) under the astrocyte-special *Gfap* promoter was injected bilaterally into the substantia nigra of mice (0.25 μL/min, 1 μL). The injection coordinates were as follows: A/P −3.0 mm, R/L ±1.3 mm, and D/V −4.5 mm. The MPTP model was performed 3 weeks after AAV injection. The information regarding the AAVs is listed in Supporting Information Table S1.

2.6. Behavioral tests

An investigation was carried out to assess spontaneous locomotion using the open field test. The study involved mice acclimatizing to the experimental setting for a period of 3 h. Subsequently, each mouse was individually introduced into the central compartment of an opaque box measuring 50 cm × 50 cm × 40 cm, with the central area having dimensions of 35 cm × 35 cm. The entire experimental process was video-recorded for a duration of 10 min. To ensure consistency and eliminate potential olfactory cues, each opaque box was sterilized with alcohol before each trial. The analysis of the mice's behavior, specifically the frequency and duration of their presence in the central compartment, was conducted using the TopScan Real-Time Analysis software (CleverSys Inc.).

The pole test constitutes a prevalent technique for evaluating basal ganglia-associated movement disorders in murine models. This method quantifies the time required for the rodents to execute a 180-degstraight turn without succumbing to a fall, as well as the duration needed to descend from the pole's apex to its base, ensuring contact with both front claws upon landing. The assessment of motor coordination deficits is facilitated by observing prolonged durations in these tasks. The experimental setup involves a cylindrical pole with a diameter of 1 cm and a height of 50 cm. The mice undergo a training regimen comprising three trials, with each trial meticulously documenting the turn-around time and the cumulative time expended from the pole's zenith to its nadir.

The rotarod test serves as an established procedure for assessing motor coordination and equilibrium in murine subjects. Prior to the actual evaluation, the rodents underwent a training phase on an accelerating rotarod apparatus, situated in an isolated compartment. This preparatory phase is crucial for acclimatizing the mice to the rotational stimulus. Subsequently, the test was conducted at a rotational speed of 20 rpm for a duration of 180 s. The JLBehv-RRTG-5 system was employed to precisely measure and record the latency period before the mice exhibited a fall from the rotarod.

2.7. Real time quantitative and reverse transcription-PCR

The extraction of total RNA from the Substantia nigra tissue of murine subjects and astrocytes was accomplished utilizing the trizol reagent, a commercially available product from Invitrogen. Following RNA isolation, the reverse transcription process was initiated using the 5 × Hiscript II qRT supermix, a reagent provided by Vazyme. Subsequent to reverse transcription, real-time quantitative PCR (qPCR) was performed using SYBR Green Master Mix, also sourced from Vazyme. The qPCR reactions were executed on a StepOnePlus instrument, a product of Applied Biosystems. The relative quantification of gene expression was determined through the utilization of the $-\Delta\Delta CT$ and $2^{-\Delta\Delta CT}$

methods. The specific primers for the qPCR assays, which were designed and synthesized by Generay, are detailed in the Supporting Information Table S2.

2.8. Immunofluorescence and immunohistochemistry

In this investigation, we employed immunofluorescence and immunohistochemistry techniques, adhering to the methodologies previously delineated in our earlier research[14]. Astrocytes and brain tissue sections (frozen, 30 μm) were immobilized in 4% paraformaldehyde, subsequently subjected to a blocking phase with 5% BSA in PBST (0.3% Triton X-100), and incubated overnight with the designated primary antibodies at 4 °C. Following this, the appropriate secondary antibodies were introduced for 1 h at room temperature. The quantification of fluorescence intensity was accomplished using Image J software (version 1.8.0), where a uniform color threshold was established across all images, and background fluorescence was subtracted using the "analyze particles" function. Stereological analysis was conducted to determine cellular density, utilizing the optical fractionator technique (Stereo Investigator 7, MBF Bioscience). For each sixth coronal frozen section, the midbrain substantia nigra pars compacta (SNpc) was demarcated at a lower magnification (40 ×), with a counting frame measuring 50 μm by 50 μm, and a sampling grid size of 100 μm by 100 μm. All stereological assessments were performed under a 200 × magnification on an Olympus BX52 microscope (Olympus America Inc.). The primary and secondary antibodies utilized in this study are detailed in Supporting Information Table S3.

2.9. RNA scope in situ hybridization

Frozen brain sections were mounted on slides, baked at 60 °C, and fixed in 4% paraformaldehyde. Tissues were dehydrated in an ethanol series and treated with RNA scope hydrogen peroxide and target retrieval reagents. Sections were blocked and incubated with a primary antibody for GFAP overnight at 4 °C. After washing, the tissues were treated with RNA scope Protease Plus and hybridized with an *Fgf7* probe mix at 40 °C for 2 h. The signal was amplified using the RNA scope multiplex fluorescent detection reagents, followed by incubation with a fluorescently-labeled secondary antibody. Slides were mounted for microscopic imaging.

2.10. Reconstruction of astrocyte morphology and sholl analysis

The images were imported into Fiji software (1.53q), and reconstruction was performed using the simple neurite tracer plugin[31]. Only astrocytes that exhibited fully intact GFAP-immunostained processes were selected for reconstruction (23−26 astrocytes were reconstructed and analyzed per group). Morphological analysis was performed using sholl analysis plugin[32], and the number of intersections was counted between the astrocytic processes and concentric spheres emanating from the cell soma.

2.11. Cell culture and treatment

Astrocytes were isolated following the methods previously described[33]. In this study, the neonatal mouse Substantia nigra tissue, comprising wild-type (WT), *Arrb1* knockout (KO), and *Arrb2* knockout (KO) specimens, was subjected to enzymatic dissociation using 0.25% trypsin at 37 °C. The enzymatic dissociation process was halted by the addition of DMEM (#11965092, Gibco) supplemented with 10% Fetal Bovine Serum (FBS) and 1% penicillin/streptomycin. Subsequently, the dissociated cells were cultured on flasks and transferred to fresh medium 24 h post-dissociation, with periodic medium changes every three days. HEK-293T cells were cultured in DMEM supplemented with 10% FBS and 1% penicillin/streptomycin. Neurotoxic astrocyte model was established by treating astrocytes with IL-1α (3 ng/mL), TNF (30 ng/mL), and C1q (400 ng/mL) for 24 h. In this study, astrocytes were cultured in serum-containing culture medium and switched to serum-free medium prior to conducting any experiments. Our cultured astrocytes maintain a high level of purity, with a negligible presence of IBA1-positive microglia. Astrocytes were incubated with various reagents, including MPP^+ (500 μmol/L, 24 h), FGF7 (0−200 ng/mL, 0−72 h), BGJ398 (0−4 μmol/L, 24 h), 3-MA (5 mmol/L, 6 h), MG132 (10 mmol/L, 6 h), UNC9995 (10 μmol/L,1 h) and dbcAMP (100 μmol/L, 3 h), as described in the corresponding figure legends. Primary substantia nigra neurons were cultured using a well-established protocol as previously described[33]. The substantia nigra region was meticulously excised from the brain tissue using cold PBS. Following this, the tissue was subjected to enzymatic dissociation using 0.25% trypsin for a duration of 12 min at 37 °C. The dissociated cells were then seeded onto culture dishes that had been pre-coated with poly-D-lysine. After a 4-h incubation period in a 5% CO_2 incubator at 37 °C, the medium was replaced with serum-free Neurobasal medium (#21103049, GIBCO) that was supplemented with B27 and glutamine. The culture medium was refreshed with half of the original volume every 3 days. The neurons used in the experiment were derived from cultures that had been maintained for 12−14 days *in vitro* (DIV). Neurons were exposed to conditioned medium collected from astrocytes for a period of 24 h. Following this, the neurons were subjected to MAP2 immunofluorescence assay, and all the reagents and resources utilized in the experiment were detailed in Table S3.

2.12. Cell transfection and plasmid construction

Primary astrocytes were cultured in 6-well plates and subjected to transfection with siRNA targeting *Arrb2*, *Fgf7*, *Fgfr2*, *Stat1*, *Rnf220* (Jima, China) using siRNA-Mate. Plasmids of pcDNA3.1-*Stat1*, *His-Ub*, and *Arrb2* were co-transfected into astrocytes or HEK-293T cells using lipofectamine 3000 reagent from Invitrogen. Cells were collected for experiments after transfection for a period of 48 h. The sequences of siRNAs were detailed in Table S2. Plasmids encoding full length and truncated forms of RNF220 were constructed. EcoR1 and Xba1 were used to linearize the pcDNA3.1-3 × Flag vector plasmid, and the amplified target fragment was inserted into the linearized vector. After monoclonal screening, the recombinant was sequenced and found to be consistent with the amplified sequence, making it suitable for transfection.

2.13. Cell viability assay

Cell viability was assessed using CCK-8 kits from Selleckin accordance with the instructions of manufacturer. Specifically, astrocytes were seeded into a 96-well plate at a density of 5000 cells/well. Following the desired treatments, cells were incubated with the reagent for 1 h. Following this incubation period, the plate was gently shaken on an orbital shaker for 1 min. The absorbance at 450 nm was then measured using the Multiskan

Spectrum (Thermo Fisher Scientific) to determine the cell viability and assess the effects of the treatments on the astrocytes.

2.14. Flow cytometry assay

Following the desired treatments, astrocytes were harvested by trypsinization and washed twice with PBS. The Edu cell proliferation detection kit (Solarbio, Beijing, China) was utilized to assess astrocyte proliferation in accordance with the manufacturer's instructions. The fluorescence intensity was subsequently analyzed by flow cytometry (Guava, easycyteTM8, Merk Millipore, Billerica, MA, USA).

2.15. RNA extraction and library construction

Total RNA was isolated from wild-type and *Arrb2* KO astrocytes, which were either treated with MPP^+ or left untreated. The extraction was performed using TRIzol reagent following the manufacturer's guidelines. Subsequently, the RNA samples were assessed for both quality and quantity using a NanoDrop ND-1000 spectrophotometer. The integrity of the RNA was evaluated by analyzing the RNA Integrity Number (RIN) with a Bioanalyzer 2100, ensuring a value greater than 7.0, which was further confirmed through electrophoresis on denaturing agarose gel. Poly(A) RNA was then isolated from 1 μg of total RNA through two rounds of purification utilizing Dynabeads Oligo(dT) 25−61005. The purified poly(A) RNA was fragmented into smaller sections using the Magnesium RNA Fragmentation Module at 94 °C for 5−7 min. These cleaved RNA fragments were subsequently reverse-transcribed to generate cDNA with SuperScript™ II Reverse Transcriptase. The cDNA molecules were used to synthesize second-stranded DNAs labeled with dUTP using *E. coli* DNA polymerase I, RNase H, and dUTP solution. An A-base was added to the blunt ends of each DNA strand to enable ligation to the indexed adapters. Single- or dual-index adapters with a T-base overhang were ligated to the fragmented DNA, followed by size selection using AMPureXP beads. After treatment with a heat-labile UDG enzyme, the ligated products underwent PCR amplification with specific conditions: initial denaturation at 95 °C for 3 min, 8 cycles of denaturation at 98 °C for 15 s, annealing at 60 °C for 15 s, and extension at 72 °C for 30 s, and a final extension at 72 °C for 5 min. The resulting cDNA library had an average insert size of 300 ± 50 base pairs. Finally, paired-end sequencing of 2 × 150 base pairs (PE150) was conducted on an Illumina Novaseq™ 6000 platform (LC-Bio Technology Co., Ltd., Hangzhou, China) following the recommended protocol from the vendor.

2.16. Bioinformatics analysis of RNA-seq

The RNA-seq data underwent bioinformatics analysis, beginning with preprocessing steps using the fastp software (https://github.com/OpenGene/fastp). This tool was employed to eliminate reads containing adaptor contamination, low-quality bases, and undetermined bases, following default parameters. Subsequently, the sequence quality was assessed using fastp. The alignment of these processed reads to the *Mus musculus* (GRCm38) reference genome was achieved through HISAT2 (https://ccb.jhu.edu/software/hisat2). The resultant alignments were then utilized for transcript assembly using StringTie (https://ccb.jhu.edu/software/stringtie) with default settings. A consolidated transcriptome was constructed by merging the individual sample transcriptomes using gffcompare (https://github.com/gpertea/gffcompare/). StringTie was further utilized to estimate the expression levels of all transcripts and to conduct expression analysis for mRNAs, calculating FPKM values based on Eq. (1):

FPKM = [Total_exon_fragments/mapped_reads (millions) × Exon_length (kB)] (1) Differential expression analysis was performed by selecting mRNAs with a fold change greater than 2 or less than 0.5, alongside a parametric F-test comparing nested linear models (P value < 0.05), executed using the R package edgeR (https://bioconductor.org/packages/release/bioc/html/edgeR.html). For subsequent bioinformatic analyses including principal component analysis, Venn diagrams, heatmaps, and gene ontology (GO) enrichment, OmicStudio tools available at https://www.omicstudio.cn/tool were employed.

2.17. Label-free mass spectrometry

Label-free mass spectrometry was carried out following established protocols[34]. The immunoprecipitated proteins (500 μg per sample) from anti-β-Arrestin2 and anti-STAT1 were processed using the FASP technique. To eliminate detergents and other low-molecular-weight substances, the protein solution was subjected to multiple ultrafiltrations with 200 μL UA buffer *via* centrifugation. Following this, the proteins were digested with 3 μg of trypsin and 40 μL of 25 mmol/L NH_4HCO_3 overnight at 37 °C. After digestion, the peptides were desalted using C18 cartridges, concentrated by vacuum centrifugation, and then reconstituted in 40 μL of 0.1% (*v*/*v*) trifluoroacetic acid. The mass spectrometry (MS) experiments were performed using a Q Exactive mass spectrometer linked to an Easy nLC system. Peptides (5 μg) were separated on a C18-reversed-phase column with a linear gradient of buffer B (80% acetonitrile and 0.1% formic acid) at a flow rate of 250 nL/min, using IntelliFlow technology over 120 min in buffer A (2% acetonitrile and 0.1% formic acid). Data were collected using a data-dependent top10 method, selecting the most abundant precursor ions from the survey scan (*m*/*z* 300−1800) for HCD fragmentation. The target value was determined using predictive automatic gain control. Survey scans were performed at a resolution of 70,000 at *m*/*z* 200, while the resolution for HCD spectra was set to 17,500 at 200 *m*/*z*. The peptide recognition mode was activated during the MS operation. Each sample was analyzed in triplicate using MS data, which were searched against the UniProtKB database and processed with MaxQuant software version 1.3.0.5.

2.18. Western blotting analysis

Cells and brain tissues were lysed using a RIPA buffer, which was supplemented with a protease phosphatase inhibitor cocktail to prevent degradation of the proteins. The samples were subsequently subjected to centrifugation at 13,000 rpm for 20 min at 4 °C to separate the cellular components. The protein concentration was quantified using the Beyotime Micro BCA Kit. The proteins extracted from the lysates were then separated based on molecular weight using SDS-PAGE, employing a gradient gel ranging from 8% to 12%. Following electrophoretic transfer of the proteins onto polyvinylidene difluoride (PVDF) membranes, a blocking step was performed to minimize non-specific binding. The membranes were then incubated with primary antibodies specific to the target proteins overnight at 4 °C. After thorough washing to remove unbound antibodies, the membranes were exposed to horseradish peroxidase (HRP)-conjugated secondary antibodies for 1 h at room temperature. The subsequent detection of the bound antibodies was achieved using Pierce detection

reagents, and the resulting protein bands were visualized and analyzed using the GE Healthcare ImageQuant™ LAS 4000 imaging system. The primary and secondary antibodies utilized in this study are detailed in Table S3.

2.19. Co-immunoprecipitation (Co-IP) assay

The cells were broken down using NP-40 buffer, and the proteins were captured using particular primary antibodies and Magnetic Beads with Protein G. Following the manufacturer's guidelines, the proteins were then separated from the beads. For Western blotting, the samples were heated at 95 °C for 10 min.

2.20. Proximity ligation assay (PLA)

To detect protein interactions in astrocytes, the Duolink PLA assay kit (Sigma−Aldrich, DUO92101) was utilized in accordance with the manufacturer's protocol. Astrocytes were fixed using 4% paraformaldehyde and permeabilized with 0.3% Triton X-100 in PBS. The cells were then blocked by incubation with blocking solution at 37 °C for 1 h. Next, the astrocytes were incubated with specific primary antibodies overnight at 4 °C, followed by incubation with PLA probe solution for 1 h at 37 °C. After washing, the astrocytes were placed at 37 °C for 30 min, followed by incubation with the amplification solution at 37 °C for 100 min, protected from light. The nucleus was subsequently observed with DAPI staining, and the cells were visualized under confocal microscopy.

2.21. ELISA assay

The levels of FGF7, IL-1β, TNF-α, and IL-6 in culture medium from astrocytes were measured by ELISA kits following the manufacturer's instructions.

2.22. Chromatin immunoprecipitation (ChIP) assay

ChIP assays were performed using a ChIP Assay Kit (Millipore, 17−295) following the manufacturer's instructions. Briefly, we retrieved the promoter region of *Fgf7* from PubMed (https://www.ncbi.nlm.nih.gov/) and predicted the STAT1 binding sequences using JASPAR (https://jaspar.elixir.no/). Sequences with scores above 10 were selected, and after removing duplicates, motif-1 (399−412 bp) and motif-2 (1199−1213 bp) were chosen for further study. DNA-protein crosslinking occurred by treating astrocytes with 1% formaldehyde and protease inhibitors at 37 °C for 20 min. Glycine at 125 mmol/L was added to halt formaldehyde action, followed by a 5-min room temperature incubation. DNA was immunoprecipitated from sonicated cell lysates using anti-STAT1 or anti-IgG antibodies, and quantified *via* RT-qPCR. *Fgf7* promoter primer sequences are as follows:

Motif-1:
Forward: GAGCACAGAGCAGGGAACTC.
Reverse: GGAGTGTTCGCAATGTTGG.
Motif-2:
Forward: CAGTCTTGCTCAGTACAGGATAGG.
Reverse: ACCGGACTGGGATTCTAACA.

2.23. Prediction of transcription factors for Fgf7

The *Fgf7* gene was input into three different databases: Animal TFDB, Genecards, and the Promo database. Subsequently, we compiled the suggested transcription factors predicted by each database, namely 548 from Animal TFDB, 306 from Genecards, and 428 from the Promo database. To narrow down these results, we constructed a Venn diagram to determine common transcription factors across all three databases. This process resulted in the identification of the nine common transcription factors.

2.24. Luciferase reporter assay

The HEK-293T cells were seeded onto a 24-well plate and cultured until they reached 70% confluence to facilitate transfection. Plasmids encoding negative control, STAT1, as well as WT-FGF7 and Mutant-FGF7 plasmids were co-transfected based on the experimental design. To assess transfection efficiency, cells were transfected with PRL-TK *Renilla* luciferase control reporter plasmid. After 48 h, luciferase assays were conducted by Dual-Luciferase^{R} Reporter Assay System kit (Promega). *Renilla* luciferase activity was measured by GLOMAX 20/20 LUMINOMETER (Promega).

2.25. Simulation of the interaction between β-Arrestin2 and RNF220

The three-dimensional structure of β-Arrestin2 (PDB ID: 3P2D) was obtained from the RCSB Protein Data Bank, while the structure RNF220 was obtained *via* homology modeling using SWISS-MODEL. ZDOCK module of Discovery Studio was used to explore the interaction between β-Arrestin2 and RNF220. β-Arrestin2 was designated as the ligand, and RNF220 was utilized as the receptor, with a final angular step size of 6 for conformational sampling. The most favorable ZDOCK and RDOCK scores were utilized to choose the ultimate docked conformations from both docking procedures. The visual representations were produced using PyMOL version Open-Source 1.6.x.

2.26. Statistical analysis

Data analysis was carried out by GraphPad Prism 8.0.0 software. Unpaired Student's *t*-test was performed to compare a single variable between two groups. When analyzing a single variable across three or more groups, one-way analysis of variance (ANOVA) was applied, with Tukey's multiple comparisons test used for *post hoc* analysis. In scenarios involving comparisons between two independent variables, two-way ANOVA was conducted, followed by Tukey's multiple comparisons test. Graphs were generated to depict the mean along with 95% confidence intervals (CI), with individual data points included. Statistical significance was defined as $P < 0.05$. *In vitro* experiments were conducted with a minimum of three biological replicates and two technical replicates, with further details available in the figure legends.

3. Results

3.1. Deficiency of β-Arrestin2 boosts neurotoxic astrocyte reactivity in the MPTP mouse model

Previously, we observed the potential influence of β-Arrestin2 on neuroinflammation in astrocytes within the framework of PD[28,35]. This captivating observation prompted us to delve deeper into the underlying mechanism governing β-Arrestin2-mediated astrocyte reactivity. In the present study, we identified a significant downregulation of β-Arrestin2 in MPTP-induced mice (Supporting

Information Fig. S1A). Importantly, we determined that global knockout (KO) of *Arrb2*, the gene encoding β-Arrestin2 (Fig. S1B and S1C), exacerbated the loss of DA neurons in mice induced by MPTP (Fig. S1D and S1G). Intriguingly, we noticed that *Arrb2* KO mice exhibited elevated reactivity of astrocytes at baseline, which were further intensified in the presence of MPTP treatment (Fig. S1E and S1H). Additionally, *Arrb2* KO contributed to microglia reactivity solely in the context of MPTP treatment (Fig. S1F and S1I). Collectively, the aforementioned results denote that the absence of β-Arrestin2 exacerbates astrocyte reactivity, potentially augmenting MPTP-induced pathology.

To explore the specific regulatory function of β-Arrestin2 in astrocyte reactivity, we generated mice with astrocytic *Arrb2* conditional knockdown (cKD) by injecting AAV2/9-*Gfap*-mir30-*m-Arrb2-Egfp* into the Substantia nigra region (Fig. 1A). The protein level of β-Arrestin2 was dramatically decreased in the substantia nigra tissue three weeks after injection (Fig. 1B, Supporting Information Fig. S2A and S2B). Consistent with *Arrb2* KO mice, *Arrb2* cKD mice exhibited heightened astrocyte reactivity as reflected by immunostaining of both Glial Fibrillary Acidic Protein (GFAP) and S100β (Fig. 1C and D, Fig. S2C and S2D). Notably, most genes associated with astrocyte reactivity were responded to *Arrb2* cKD of MPTP-treated mice, as determined by RT-qPCR analysis of the Substantia nigra tissue (Fig. 1E and Fig. S2E). Although these genes examined are not exclusive to astrocytes due to the presence of other cell types within the brain tissue, this phenomenon was corroborated by immunofluorescence staining of substantia nigra slices, which revealed a substantial increase in $C3^+$-$GFAP^+$ cells (Fig. S2F and S2G), but not $S100A10^+$-$GFAP^+$ cells (Fig. S2H and S2I), in the *Arrb2* cKD mice. We also observed intricate morphological complexity of astrocytes through the reconstruction of individual astrocytes, displaying fully intact GFAP-immunostained processes (Fig. 1F). Sholl analysis demonstrated that astrocytes from *Arrb2* cKD mice manifested higher complexity, underlined by an increased number of intersections both in normal conditions and after MPTP treatment (Fig. 1G and H). These findings highlight the critical role of β-Arrestin2 in regulating $C3^+$-$GFAP^+$ neurotoxic astrocyte reactivity. To provide direct evidence, we next performed the well-established neurotoxic astrocyte conversion model[5,13]. As anticipated, knockdown of *Arrb2* promoted the expression of neurotoxic markers induced by IL-1α+TNF + C1q, while overexpression of *Arrb2* prevented their expression in cultured astrocytes (Fig. 1I and J). Functionally, the reactive astrocytes induced by *Arrb2* cKD/MPTP exacerbated DA neuronal loss in the Substantia nigra, as indicated by a significant reduction in tyrosine hydroxylase (TH) expression (Fig. 1K, Fig. S2J and S2K). *In vitro* experiments showed that conditioned medium from both IL-1α+TNF + C1q- and MPP^+-stimulated *Arrb2* KO astrocytes significantly damaged the dendrites of primary cultured neurons (Fig. 1L−N, Fig. S2L and S2M). These findings suggest that β-Arrestin2 is a key regulator of astrocyte reactivity, contributing to the progression of DA neuronal loss.

3.2. FGF7-accumulated astrocytes gain reactive phenotype in the absence of β-Arrestin2

Next, we aimed to investigate the potential mechanism underlying the phenotypic transformation of astrocytes mediated by β-Arrestin2. Primary astrocytes were cultured from the midbrain of neonatal WT and *Arrb2* KO mice. RNA sequencing (RNA-Seq) was performed to compare the transcriptome of astrocytes in the context of MPP^+ treatment. Principal component analysis (PCA) of the transcriptomes from 12 samples (4 groups, 3 biological replicates per group) revealed that both the genotype and MPP^+ treatment significantly influenced the astrocyte transcriptome, as evidenced by the clustering of samples based on these factors (Fig. 2A). Subsequently, we identified 509 differentially expressed genes (DEGs) using a Venn diagram (Fig. 2B), which were further analyzed in terms of their gene ontology (GO) enrichment. This analysis revealed that the DEGs were significantly associated with astrocyte reactivity, particularly in terms of positive regulation of cell proliferation and inflammatory response (Fig. 2C and D). Moreover, we performed a comprehensive comparison between the transcriptomic changes observed in reactive astrocytes from our study and the dataset GSE165069 concerning IL-1α+TNF + C1q-induced reactive astrocytes[9]. We focused on the top 500 DEGs from both datasets. This analysis revealed 39 genes that were commonly altered in both studies and 461 unique genes that differed between the two datasets (Supporting Information Fig. S3A). Furthermore, GO enrichment analysis of the shared 39 DEGs highlighted their association with processes such as inflammation, wound healing, and leukocyte activity (Fig. S3A). The analysis provided an understanding of the core functional changes that occur in neurotoxic reactive astrocytes across different conditions. Moreover, GO enrichment analysis of the 461 distinct DEGs from Philip's study primarily pinpointed chemokine and cytokine activity (Fig. S3B). Conversely, our dataset stood out for its association with growth factor binding among the unique set of 461 differentially expressed genes (Fig. S3C).

To delve deeper into the role of specific DEGs in astrocyte reactivity within our experimental settings, we selected the top 10 DEGs associated with the aforementioned GO terms (Fig. 2E) and validated their expression levels using RT-qPCR (Fig. 2F). Among these genes, *Fgf7* exhibited the most significant increase in response to both *Arrb2* KO and 1-methyl-4-phenylpyridinium (MPP^+) treatment in cultured astrocytes (Fig. 2F). Western blotting analysis confirmed that the protein level of FGF7 was significantly increased in both *Arrb2* KO and MPP^+-stimulated conditions, concomitant with increased levels of GFAP and proliferating cell nuclear antigen (PCNA), indicating enhanced astrocyte reactivity and proliferation (Fig. 2G, Fig. S3D and S3E). This observation was further validated by immunofluorescence staining of GFAP, FGF7, and EdU in cultured astrocytes (Fig. S3F and S3G). Consistently, *Arrb2* cKD mice had elevated FGF7 levels compared to WT mice under both basal and MPTP-induced conditions (Fig. S3H). Importantly, the upregulation of *FGF7* was also observed in the post-mortem substantia nigra tissue[19] and induced pluripotent stem cells (iPSCs)-derived astrocytes from PD patients[36], extending the relevance of our findings to PD more broadly (Fig. S3I and S3J). Next, we examined the cellular expression patterns of FGF7 and its receptor FGF receptor 2 (FGFR2) in the MPTP model. Immunofluorescence staining of Substantia nigra slices targeting FGF7 and FGFR2 along with GFAP and Ionized calcium-binding adapter molecule 1 (IBA-1) in the substantia nigra region demonstrated that both under physiological and MPTP conditions, FGF7 and FGFR2 are primarily expressed in astrocytes (Fig. 2H and I), with some expression in microglia (Supporting Information Fig. S4A and S4B). Through RNA scope analysis, we validated that a substantial increase in *Fgf7* expression was identified predominantly in astrocytes following MPTP treatment (Fig. 2J). Remarkably, in the neurotoxic astrocyte conversion model, knockdown of *Fgf7* reduced the expression levels of neurotoxic markers in both WT and *Arrb2* KO cultured astrocytes (Fig. 2K). This observation was further

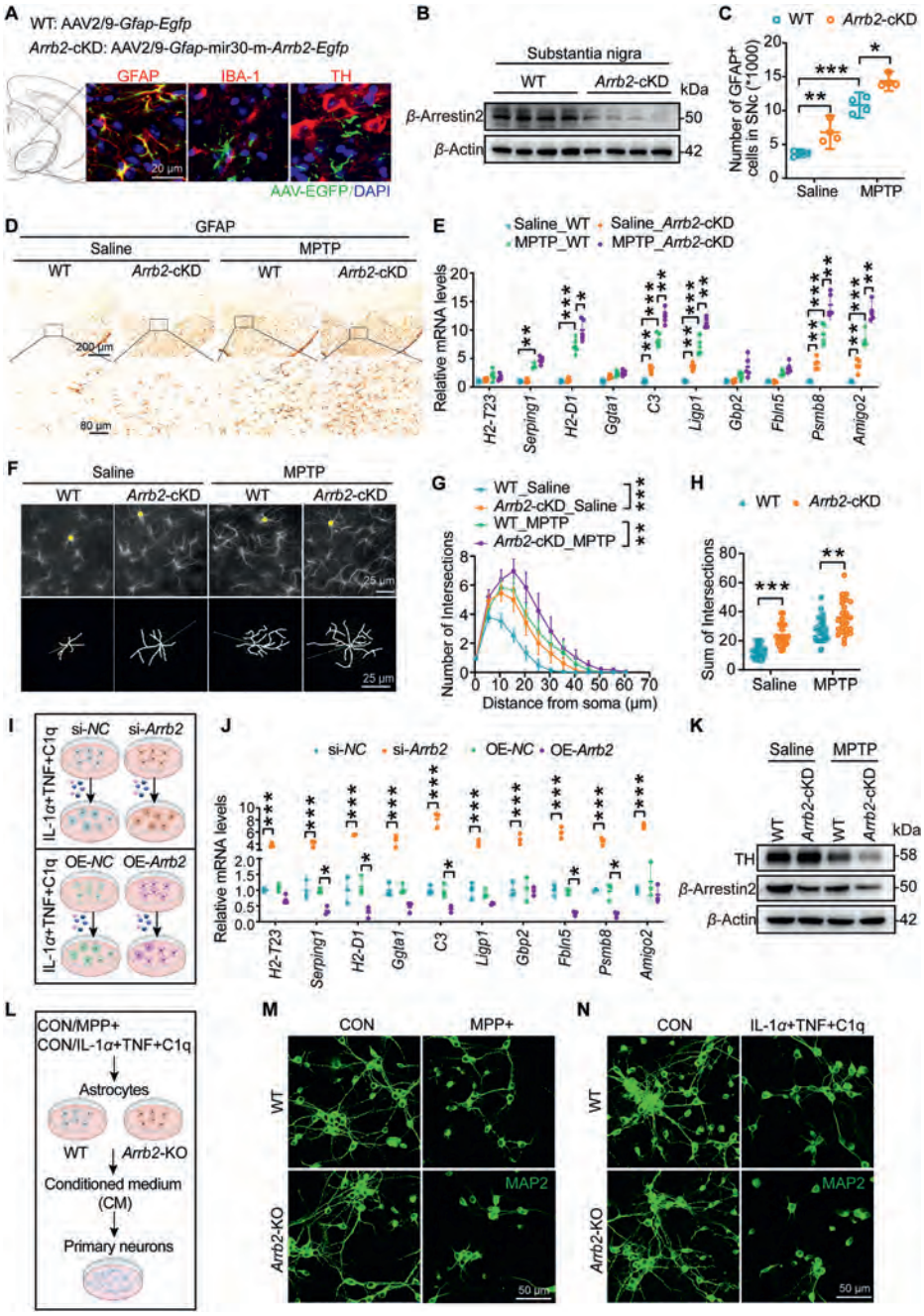

Figure 1 β-Arrestin2 deficiency enhances astrocyte reactivity in the MPTP model. (A) Schematic representation of AAV injection site, visualized green for EGFP and red for GFAP/IBA-1/TH. Scale bar: 20 μm. (B) Representative immunoblot of β-Arrestin2 in the substantia nigra tissue of WT and *Arrb2* cKD mice. (C, D) Quantification and representative images of GFAP positive cells in substantia nigra slices. Scale bar: 200 μm (upper panel), 80 μm (lower panel). $^{*}P < 0.05$, $^{**}P < 0.01$, $^{***}P < 0.001$ by two-way ANOVA with Tukey's multiple comparisons test, $n = 4$ per group. (E) RT-qPCR analysis of the mRNA levels of neurotoxic markers in the substantia nigra tissue. $^{*}P < 0.05$, $^{**}P < 0.01$, $^{***}P < 0.001$ by two-way ANOVA with Tukey's multiple comparisons test, $n = 5$ per group. (F) Reconstruction of individual astrocytes in the SNc region. Scale bar: 25 μm. (G, H) Quantification of the intersections from reconstructed astrocytes by Sholl analysis. $^{**}P < 0.01$, $^{***}P < 0.001$ by two-way ANOVA with Tukey's multiple comparisons test, $n = 23-26$. (I, J) RT-qPCR analysis of the effects of *Arrb2* knockdown and overexpression on neurotoxic markers in the IL-1α+TNF + C1q-induced neurotoxic astrocyte model. $^{*}P < 0.05$, $^{***}P < 0.001$ by two-way ANOVA with Tukey's multiple comparisons test, $n = 3$. Astrocytes were incubated with IL-1α (3 ng/mL), TNF (30 ng/mL), and C1q (400 ng/mL) for 24 h. (K) Representative blots showing the expression of TH and β-Arrestin2 in Substantia nigra tissue. (L−N) Immunofluorescence staining of MAP2 showing the effects of conditioned medium collected from astrocytes on neuronal survival. Scale bar: 50 μm.

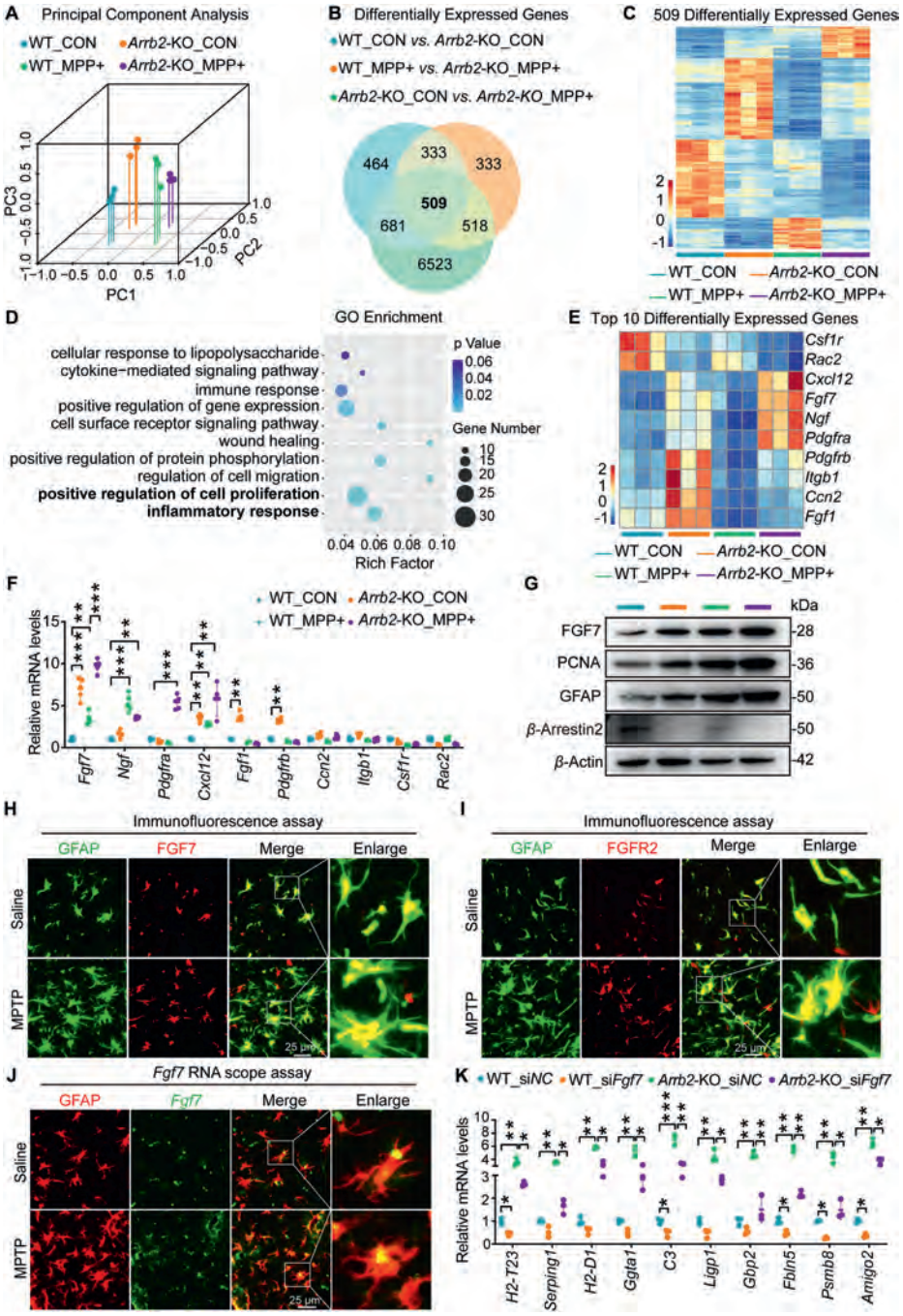

Figure 2 FGF7 overproduction in the absence of β-Arrestin2 boosts astrocyte reactivity. (A) Principal component analysis of transcriptomes from WT and *Arrb2* KO astrocytes in basal and MPP $^{+}$ treatment (500 μmol/L, 24 h), $n = 3$ biological replicates. (B) Venn diagram showing the number of differentially expressed genes between 2 groups and the overlap of differentially expressed genes among the 3 comparisons. (C) Heatmap of the overlapped 509 differentially expressed genes. (D) Gene ontology biological process enrichment analysis of the overlapped 509 differentially expressed genes. (E) Heatmap of the top 10 differentially expressed genes associated with GO terms of positive regulation of cell proliferation and inflammatory response. (F) RT-qPCR analysis of the selected top 10 differentially expressed genes. $^{**}P < 0.01$, $^{***}P < 0.001$ by two-way ANOVA with Tukey's multiple comparisons test, $n = 5$. (G) Representative blots of FGF7, PCNA, GFAP, and β-Arrestin2 in WT and *Arrb2* KO astrocytes in basal and MPP $^{+}$ treatment. (H, I) Immunofluorescence of FGF7, FGFR2, and GFAP in Substantia nigra slices. Scale bar: 25 μm. (J) *Fgf7* RNA scope assay demonstrating the presence of *Fgf7* in astrocytes in Substantia nigra slices. Scale bar: 25 μm. (K) RT-qPCR analysis of the effect of *Fgf7* on neurotoxic markers in *Arrb2* KO astrocytes treated with IL-1α+TNF + C1q. $^{*}P < 0.05$, $^{**}P < 0.01$, $^{***}P < 0.001$ by two-way ANOVA with Tukey's multiple comparisons test, $n = 3$.

supported by Western blotting analysis of C3 expression (Fig. S4C and S4D). Taken together, we speculate that the overproduction of FGF7, resulting from either β-Arrestin2 deficiency or MPP^+ stimulation, drives astrocytes towards a reactive phenotype.

3.3. FGF7/FGFR2 autocrine signaling drives astrocyte proliferation and inflammatory phenotype

To examine the hypothesis, cultured astrocytes were treated with exogenous FGF7 for varying concentrations and time spans. Astrocytes treated with FGF7 at 20 ng/mL for 24 h exhibited higher cell viabilities than control astrocytes, suggesting the potential effect of FGF7 on astrocyte proliferation (Fig. 3A and B). Noteworthy, FGF7 (20 ng/mL, 24 h) promoted the proliferation (increased level of PCNA) and reactivity (increased level of GFAP) of astrocytes under both basal and MPP^+ treatment conditions (Fig. 3C and Supporting Information Fig. S5A). The effect of FGF7 on astrocyte proliferation was confirmed by Flow cytometry analysis of Edu (Fig. 3D and E). Importantly, FGF7 treatment promoted the release of proinflammatory cytokines, including IL-1β, TNF-α, and IL-6, from astrocytes under both basal and MPP^+ treatment conditions (Fig. 3F). Furthermore, the addition of FGF7 increased C3 expression in the neurotoxic astrocyte model (Fig. 3G and H). We identified that NF-κB signaling, but not signal transducer and activator of transcription 3 (STAT3) signaling, was involved in the FGF7-induced neurotoxic phenotype of reactive astrocytes (Fig. S5B and S5C). FGF7 is known to be a specific ligand of FGFR2, and we found that knockdown of *Fgfr2* inhibited the upregulation of PCNA, GFAP, and Edu in astrocytes treated with either FGF7 or MPP^+ (Fig. S5D−S5F and Fig. 3I−L). Notably, knockdown of *Fgfr2* declined the expression of C3 in the neurotoxic astrocyte model (Fig. 3M and N, Fig. S5G). Therefore, we propose that activation of FGF7/FGFR2 signaling leads astrocytes to adopt a reactive phenotype.

To validate this hypothesis, we performed knockdown of *Fgf7* and inhibition of FGFR2 in astrocytes. Consistently, we found that knockdown of *Fgf7* ameliorated MPP^+-induced proliferation and reactivity of astrocytes by inactivating NF-κB signaling (Fig. S6A−S6F). Meanwhile, knockdown of *Fgf7* reduced the expression of C3 in the neurotoxic astrocyte model (Fig. S6G−S6I). Furthermore, we applied BGJ398, a pan-FGF receptor blocker, to astrocytes to inhibit FGF signaling. Treatment with BGJ398 at 2 μmol/L for 24 h had no effect on cell viability but blocked FGF7-induced upregulation of PCNA and GFAP in astrocytes (Supporting Information Fig. S7A and S7B). Consistent with *Fgfr2* knockdown, BGJ398 blocked astrocyte proliferation and reactivity in either FGF7 or MPP^+ treatment conditions (Fig. S7C−S7G). To directly validate the role of FGF7 in astrocyte reactivity, FGF7 was injected into the substantia nigra of mice. Our results showed that FGF7 treatment enhanced astrocyte reactivity and increased the levels of pro-inflammatory cytokines (Supporting Information Fig. S8A−S8C). Collectively, these findings confirm that activation of FGF7/FGFR2 signaling triggers the transformation of astrocytes into a reactive phenotype.

3.4. Knockdown of astrocytic Fgf7 and Fgfr2 confers a positive outcome in MPTP-treated mice by reducing the presence of reactive astrocytes

We then aimed to explore the potential therapeutic benefits of attenuating astrocytic FGF7/FGFR2 signaling in the MPTP mouse model. To achieve this, we generated mice with conditional knockdown of astrocytic *Fgf7* and *Fgfr2* (cKD) by injecting AAV-*Gfap-Fgf7*/*Fgfr2* shRNA into the Substantia nigra. After a 3-week period, the mice were subjected to the MPTP model, and behavioral tests were conducted (Supporting Information Fig. S9A). The injection area and virus distribution were assessed, and a decrease in FGF7 expression was observed in *Fgf7* cKD mice (Fig. S9B−S9D). Similar observations were confirmed in *Fgfr2* cKD mice (Fig. S9E). In the open field test, the movement speed of MPTP-treated mice was increased upon knockdown of astrocytic *Fgf7* or *Fgfr2* compared to the MPTP group (Fig. 4A and B). In the pole test, knockdown of astrocytic *Fgf7* or *Fgfr2* shortened the time spent by MPTP-treated mice in total and turn around (Fig. 4C and D). In the rotarod test, astrocytic knockdown of *Fgf7* or *Fgfr2* improved the performance of MPTP-treated mice, resulting in more time spent on the rod (Fig. 4E). Importantly, knockdown of astrocytic *Fgf7/Fgfr2* rescued the loss of DA neurons induced by MPTP (Fig. 4F and G) and mitigated astrocyte reactivity (Fig. 4H and I). Notably, in the MPTP model, *Fgf7* cKD and *Fgfr2* cKD mice exhibited a lower number of reactive astrocytes relative to WT mice, as evidenced by RT-qPCR analysis of neurotoxic and neuroprotective markers (Fig. 4J and Fig. S9F). This was further supported by measuring the protein levels of C3, TH, PCNA, and GFAP in the middle brain tissue (Fig. 4K and L). These results collectively indicate that dampening astrocytic FGF7/FGFR2 signaling confers neuroprotection against MPTP-induced pathology through reducing the number of reactive astrocytes.

3.5. Astrocytic Fgf7 deletion ameliorates MPTP-induced pathology in β-Arrestin2 deficient mice

Given that astrocytes produced more FGF7 in the absence of β-Arrestin2, we sought to investigate the impact of astrocytic FGF7 on MPTP-induced pathology in *Arrb2* KO mice. Knockdown of astrocytic *Fgf7* was performed in *Arrb2* KO mice by injecting AAV2/9-*Gfap*-mir30-*m-Fgf7-Egfp* into the Substantia nigra region. Immunofluorescence staining confirmed specific virus infection in astrocytes within the Substantia nigra, and a decrease in FGF7 expression was observed in the Substantia nigra tissue (Fig. 5A and B). In the open field test, knockdown of astrocytic *Fgf7* increased the movement speed of *Arrb2* KO mice treated with MPTP (Fig. 5C and D). In the pole test, knockdown of astrocytic *Fgf7* reduced the time spent by MPTP-treated *Arrb2* KO mice in both total and turn around (Fig. 5E and F). In the rotarod test, astrocytic knockdown of *Fgf7* increased the time spent on the rod by MPTP-treated *Arrb2* KO mice (Fig. 5G). These results indicate that astrocytic *Fgf7* acts as a detrimental factor that exacerbates PD-like motor symptoms in the absence of *Arrb2*. Moreover, deletion of astrocytic *Fgf7* protected against MPTP-induced damage to DA neurons in *Arrb2* KO mice (Fig. 5H and I). As expected, we observed that the reactivity of astrocytes under both *Arrb2* KO and MPTP treatment conditions were hindered by deletion of astrocytic *Fgf7* (Fig. 5J and K). RT-qPCR analysis of neurotoxic and neuroprotective markers revealed that knockdown of astrocytic *Fgf7* reduced the elevated number of neurotoxic reactive astrocytes in *Arrb2* KO mice treated with MPTP (Fig. 5L and Fig. S9G). Consistently, the increased expression of C3, PCNA, GFAP, and the decreased expression of TH were also diminished by deletion of astrocytic *Fgf7* in *Arrb2* KO mice treated with MPTP (Fig. 5M and N). Therefore, we conclude that FGF7, acting as a downstream effector in the absence of β-Arrestin2, drives astrocytes towards a reactive phenotype, thereby exacerbating MPTP-induced pathology.

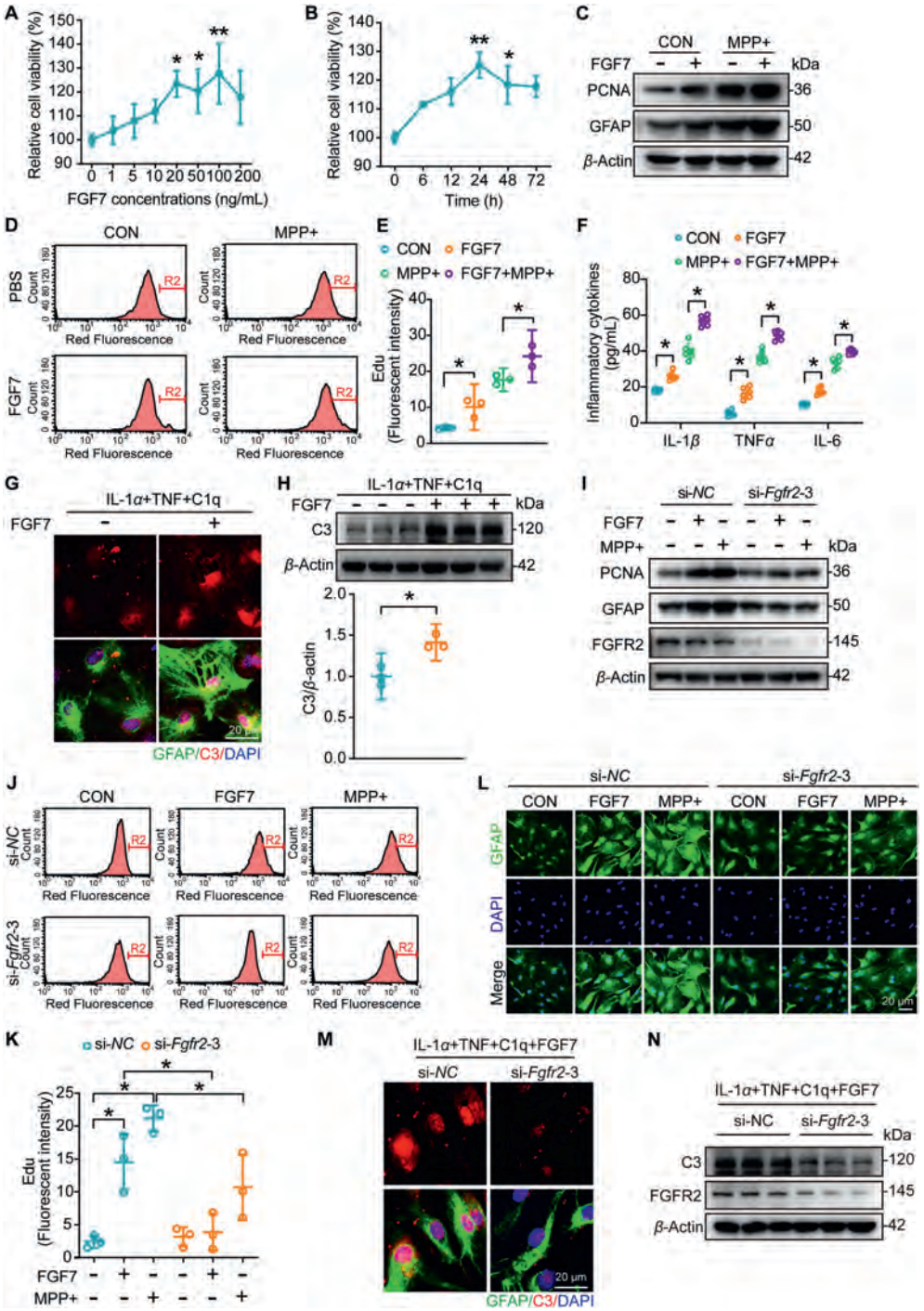

Figure 3 FGF7/FGFR2 signaling promotes astrocytes proliferation and reactivity. (A, B) CCK-8 assay showing the effects of different concentrations of FGF7 (0−200 ng/mL) and the time course effects of FGF7 treatment (20 ng/mL) on cell viability of astrocytes. $^{*}P < 0.05$, $^{**}P < 0.01$ *vs*. corresponding control group by one-way ANOVA with Tukey's multiple comparisons test, $n = 3$. (C) Representative immunoblots of PCNA and GFAP showing the effect of FGF7 (20 ng/mL, 24 h) on astrocyte proliferation and reactivity. (D, E) Representative images and quantification of Edu by flow cytometry in astrocytes treated with FGF7 (20 ng/mL, 24 h). $^{*}P < 0.05$ by one-way ANOVA with Tukey's multiple comparisons test, $n = 3$. (F) ELISA assay showing the effects of FGF7 treatment (20 ng/mL, 24 h) on the release of inflammatory cytokines including IL-1β, TNFα and IL-6 from astrocytes. $^{*}P < 0.05$ by one-way ANOVA with Tukey's multiple comparisons test, $n = 6$. (G) Immunofluorescence of C3 and GFAP in IL-1α+TNF + C1q-induced neurotoxic astrocytes treated with or without FGF7 (20 ng/mL, 24 h). Scale bar: 20 μm. (H) Representative immunoblot and quantification of C3 in IL-1α+TNF + C1q-induced neurotoxic astrocytes treated with or without FGF7 (20 ng/mL, 24 h). $^{*}P < 0.05$ by unpaired *t* test, $n = 3$. (I) Representative immunoblots of PCNA, GFAP and FGFR2 showing the effect of *Fgfr2* knockdown on astrocyte proliferation and reactivity in FGF7 or MPP $^{+}$ treatment. (J, K) Representative images and quantification of Edu by flow cytometry in *Fgfr2* knockdown astrocytes exposed to FGF7 or MPP^{+}. (L) Immunofluorescence of GFAP showing the effect of *Fgfr2*

3.6. STAT1 represses FGF7 expression in the presence of β-Arrestin2

Next, we explored the upstream events focusing on regulating astrocytic FGF7 production. We predicted 9 transcription factors of *Fgf7* using Animal TFDB, Genecards, and Promo database (Fig. 6A). LC−MS/MS analysis of anti-β-Arrestin2 immunoprecipitation from cultured astrocytes revealed the existence of STAT1, suggesting that STAT1 may regulate FGF7 production in the presence of β-Arrestin2 (Fig. 6B). As expected, knockdown of *Stat1* significantly elevated both the mRNA and protein levels of FGF7 in cultured astrocytes (Supporting Information Fig. S10A−S10D, Fig. 6C and D). Simultaneously, higher level of secreted FGF7 protein was detected in the culture medium of astrocytes with *Stat1* knockdown (Fig. S10E). Conversely, overexpression of *Stat1* resulted in a reduction in FGF7 expression and secretion (Fig. S10F−S10H, Fig. 6E and F). These findings establish STAT1 as a negative regulator of FGF7 expression. Then, we predicted the STAT1 binding sequences using JASPAR, and motif-1 (399−412 bp) and motif-2 (1199−1213 bp) were chosen for further study (Fig. S10I). Chromatin immunoprecipitation (ChIP) experiments validated that STAT1 acted as a transcription factor binding to both motif-1 and motif-2 of the *Fgf7* promoter (Fig. 6G and H). Mutation of the binding motifs within the *Fgf7* promoter region attenuated the inhibitory effect of STAT1 on *Fgf7* promoter activity, as evidenced by luciferase reporter assays in HEK-293T cells (Fig. 6I and J). More importantly, overexpression of *Stat1* reduced the elevated level of FGF7 in *Arrb2* KO astrocytes (Fig. 6K and Fig. S10J). Meanwhile, overexpression of *Stat1* reduced astrocyte proliferation and reactivity in the MPP^+ model, thereby inhibiting the release of proinflammatory cytokines (Fig. 6L, Fig. S10K and S10L). Interestingly, while both p-STAT1 and p-STAT3 levels were diminished in the substantia nigra of MPTP-treated mice, only the loss of p-STAT1 was accentuated by the absence of astrocytic *Arrb2* (Fig. S10M and S10N), spotlighting STAT1 but not STAT3 as a pivotal molecule in modulating astrocyte reactivity within the framework of MPTP model. Thus, our data demonstrate that STAT1 functions as a transcription factor that represses *Fgf7* expression in the presence of β-Arrestin2.

3.7. Loss of β-Arrestin2 triggers STAT1 ubiquitination and proteasomal degradation

To elucidate the potential working model of β-Arrestin2/STAT1-mediated FGF7 production, we conducted proximity ligation assay and co-immunoprecipitation experiments in cultured astrocytes, which confirmed an interaction between β-Arrestin2 and STAT1 (Fig. 7A and B), consistent with the findings from LC−MS/MS analysis (Fig. 6B). In *Arrb2* KO cultured astrocytes, we observed a reduction in the protein levels of p-STAT1 and STAT1, while the mRNA level of *Stat1* remained unchanged (Fig. 7C−E). This suggests the critical role of β-Arrestin2 in maintaining STAT1 stability. For this reason, we examined the degradation process of STAT1 and found that proteasome inhibition (using MG-132), but not autophagy−lysosome pathway suppression (using 3-MA), preserved STAT1 expression in *Arrb2* KO cultured astrocytes (Fig. 7F and G), indicating the involvement of the ubiquitin−proteasome pathway in the β-Arrestin2 deficiency-induced degradation of STAT1. Additionally, we observed an upregulation of STAT1 ubiquitination in *Arrb2* KO astrocytes, whereas overexpression of *Arrb2* reduced STAT1 ubiquitination in HEK-293T cells (Fig. 7H and I). Hence, our findings suggest that β-Arrestin2 inhibits the ubiquitin−proteasomal degradation of STAT1, thereby preserving its expression.

3.8. The binding of β-Arrestin2 to RNF220 hinders STAT1 degradation

E3 ubiquitin ligase is required for the ubiquitin-proteasome system[37]. In the present study, we identified RNF220 as the E3 ubiquitin ligase responsible for STAT1 degradation by LC−MS/MS analysis in cultured astrocytes (Fig. 8A). Co-immunoprecipitation experiments confirmed an increased interaction between STAT1 and RNF220 in *Arrb2* KO astrocytes, leading to STAT1 ubiquitination (Fig. 8B−D). Conversely, knockdown of *Rnf220* prevented STAT1 degradation in *Arrb2* KO astrocytes (Fig. 8E, Supporting Information Fig. S11A−S11C). Co-Immunoprecipitation experiments revealed an interaction between β-Arrestin2 and RNF220 (Fig. 8F). To determine the binding sequence, we performed simulations of the β-Arrestin2-RNF220 interaction using the ZDOCK module of Discovery Studio 2019. The structure of β-Arrestin2 was obtained from RCSB Protein Data Bank (Fig. S11D), while the structure of RNF220 was generated through homology modeling (SWISS-MODEL) and assessed using Ramachandran plots (Fig. S11E). Two poses were selected based on ZDOCK and RDOCK scores (Fig. S11F). Our analysis identified the 123−155 aa and 363−400 aa fragments of RNF220 as potential binding sites for β-Arrestin2 (Fig. 8G). Thereafter, we constructed plasmids encoding full-length and truncated forms of RNF220 to verify the binding sites of β-Arrestin2 to RNF220 (Fig. 8H). Interestingly, β-Arrestin2 was detected in the immunoprecipitated RNF220 containing either 123−155 aa or 363−400 aa segments in HEK-293T cells (Fig. 8I). Furthermore, we observed that the 1−362 aa segment of RNF220 was required for STAT1 binding in HEK-293T cells (Fig. 8J), consistent with a previous study[38]. Collectively, we propose that β-Arrestin2 blocks the binding between RNF220 and STAT1 *via* direct binding site occupation or steric hindrance, thereby preventing RNF220-meditated ubiquitin-proteasomal degradation of STAT1.

3.9. Activating Drd2/β-Arrestin2-biased signaling improves MPTP-induced pathology through inhibiting FGF7 production and astrocyte reactivity

Our previous studies established UNC9995 as a biased agonist that activates the Drd2/β-Arrestin2 signaling pathway and enhances the scaffolding function of β-Arrestin2[39,40]. In the current investigation, we discovered that UNC9995 treatment reduced the expression of FGF7 in cultured astrocytes exposed to MPP^+ (Supporting Information Fig. S12A). Moreover, UNC9995 treatment inhibited MPP^+-induced astrocyte reactivity *via*

knockdown on astrocyte reactivity in FGF7 or MPP^+ treatment conditions. Scale bar: 20 μm. (M) Immunofluorescence of C3 and GFAP in neurotoxic astrocyte model with *Fgfr2* knockdown. Scale bar: 20 μm. (N) Representative immunoblots of C3 and FGFR2 in IL-1α+TNF + C1q-induced neurotoxic astrocytes with *Fgfr2* knockdown.

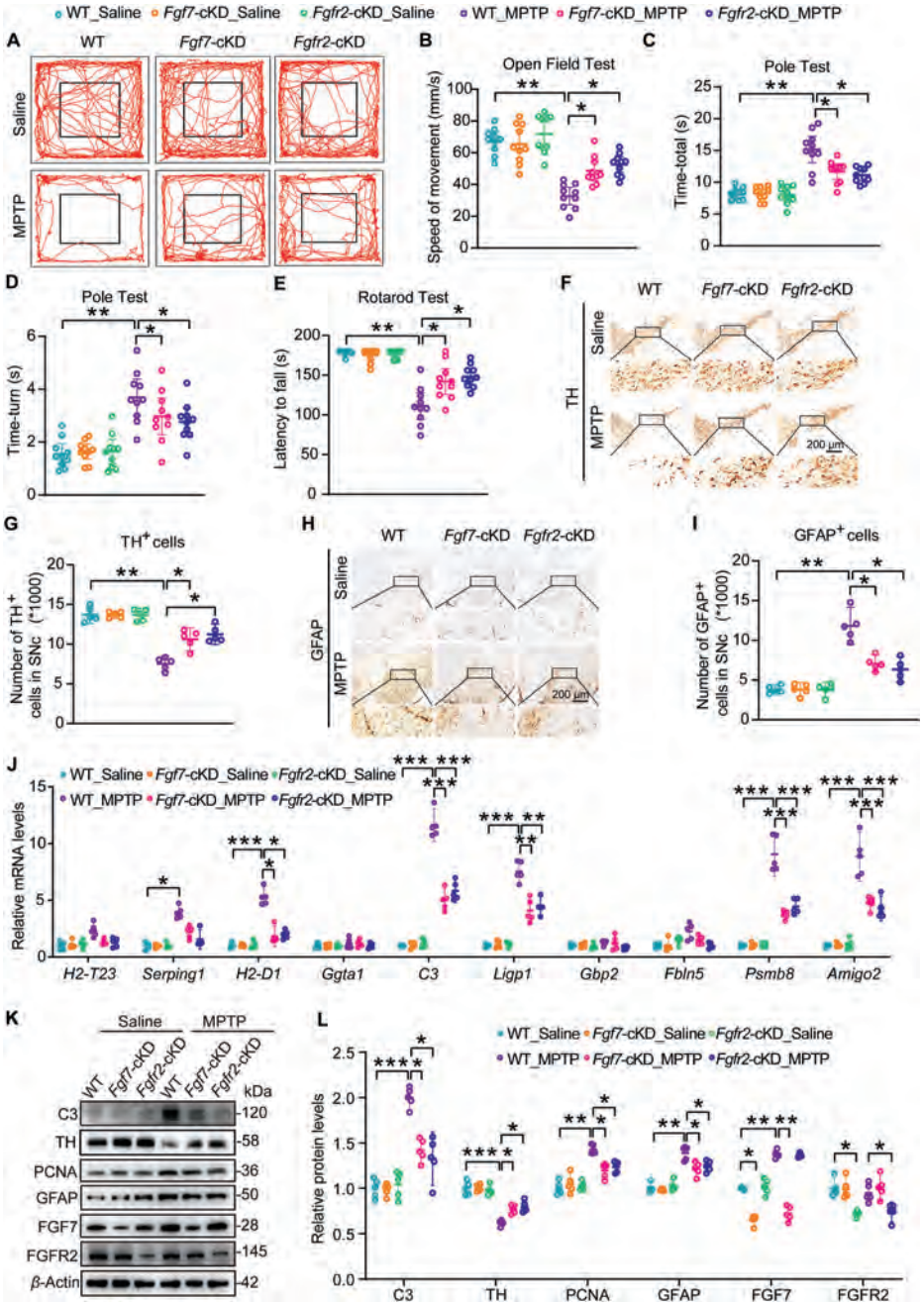

Figure 4 Knockdown of astrocytic *Fgf7* and *Fgfr2* ameliorates MPTP-induced motor symptoms and pathology through inhibition of reactive astrocytes. (A, B) Representative travel paths (red) and quantification of the movement speed in the open field test. $*P < 0.05$, $**P < 0.01$ by two-way ANOVA with Tukey's multiple comparisons test, $n = 10$. (C, D) Quantification of the total time and turn-around time spent in the pole test. $*P < 0.05$, $**P < 0.01$ by two-way ANOVA with Tukey's multiple comparisons test, $n = 10$. (E) Quantification of the latency to fall in the rotarod test. $*P < 0.05$, $**P < 0.01$ by two-way ANOVA with Tukey's multiple comparisons test, $n = 10$. (F, G) Representative images and quantification of TH immunostaining in the SNc region. Scale bar: 200 μm $*P < 0.05$, $**P < 0.01$ by two-way ANOVA with Tukey's multiple comparisons test, $n = 5$. (H, I) Representative images and quantification of GFAP immunostaining in the SNc region. Scale bar: 200 μm $*P < 0.05$, $**P < 0.01$ by two-way ANOVA with Tukey's multiple comparisons test, $n = 5$. (J) RT-qPCR analysis of the mRNA levels of neurotoxic markers in the substantia nigra tissue. $*P < 0.05$, $**P < 0.01$, $***P < 0.001$ by two-way ANOVA with Tukey's multiple comparisons test, $n = 5$. (K, L) Representative immunoblots and quantification of C3, TH, PCNA, GFAP, FGF7, and FGFR2 in the Substantia nigra tissue. $*P < 0.05$, $**P < 0.01$, $***P < 0.001$ by two-way ANOVA with Tukey's multiple comparisons test, $n = 5$.

upregulating STAT1 expression, thereby reducing the release of proinflammatory cytokines (Fig. S12B and S12C). Importantly, in the neurotoxic astrocyte model, UNC9995 treatment suppressed the expression of neurotoxic markers of reactive astrocytes (Fig. S12D). Interestingly, we observed that the addition of dbcAMP did not affect FGF7 expression in basal and MPP^+-stimulated astrocytes and failed to alter the UNC9995-induced reduction in FGF7 expression (Fig. S12E). This suggests that

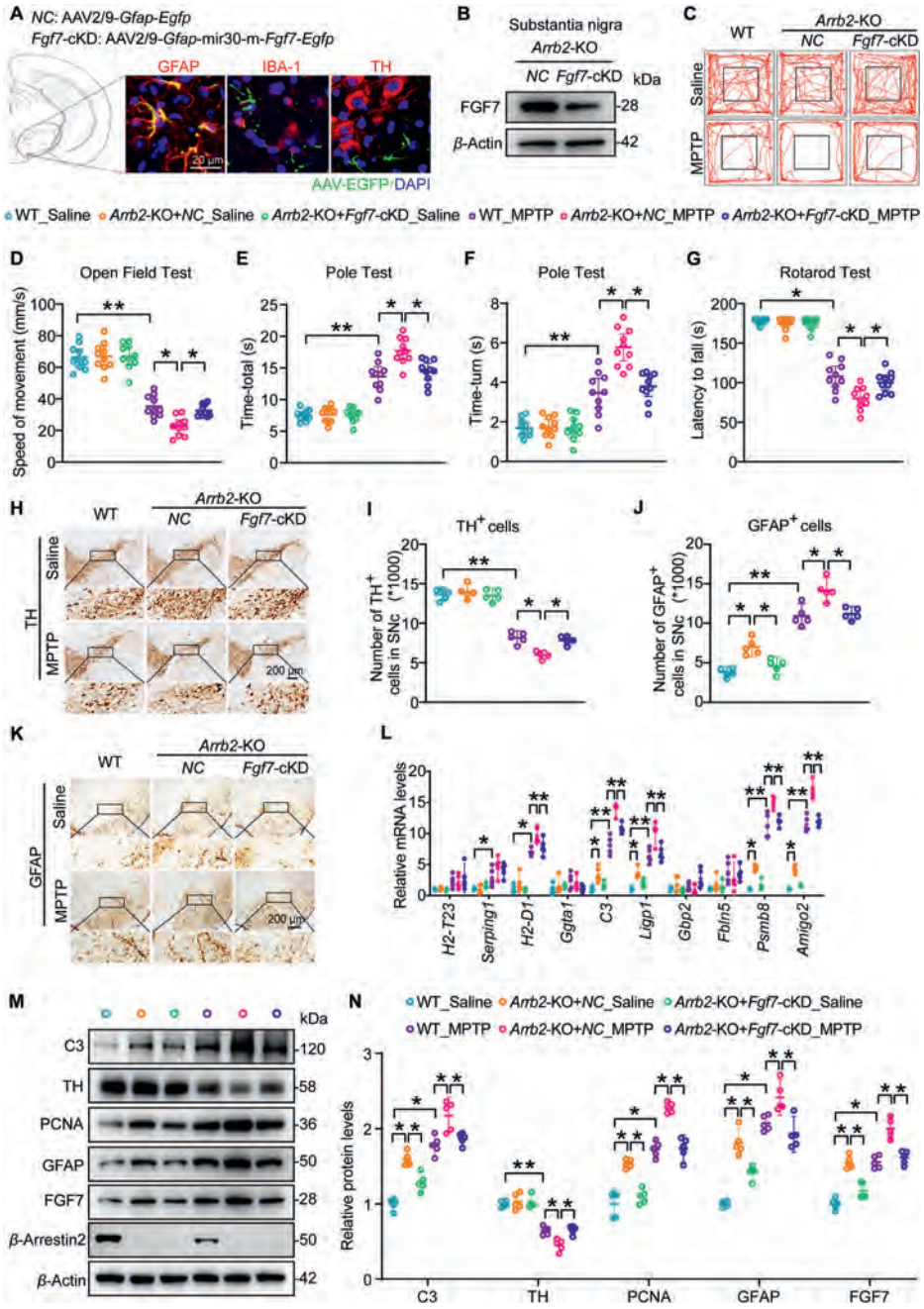

Figure 5 Knockdown of astrocytic *Fgf7* mitigates MPTP-induced motor symptoms and pathology in *Arrb2* KO mice by preventing astrocyte reactivity. (A) Schematic representation of AAV injection site, visualized green for EGFP and red for GFAP/IBA-1/TH. Scale bar: 20 μm. (B) Immunoblot of FGF7 showing a decreased protein level of FGF7 in the substantia nigra tissue of *Arrb2* KO mice. (C, D) Representative travel paths (red) and quantification of the movement speed in the open field test. $^{*}P < 0.05$, $^{**}P < 0.01$ by two-way ANOVA with Tukey's multiple comparisons test, $n = 10$. (E, F) Quantification of the total time and turn-around time spent in the pole test. $^{*}P < 0.05$, $^{**}P < 0.01$ by two-way ANOVA with Tukey's multiple comparisons test, $n = 10$. (G) Quantification of the latency to fall in the rotarod test. $^{*}P < 0.05$ by two-way ANOVA with Tukey's multiple comparisons test, $n = 10$. (H, I) Representative images and quantification of TH immunostaining in the SNc region. Scale bar: 200 μm $^{*}P < 0.05$, $^{**}P < 0.01$ by two-way ANOVA with Tukey's multiple comparisons test, $n = 5$. (J, K) Representative images and quantification of GFAP immunostaining in the SNc region. Scale bar: 200 μm $^{*}P < 0.05$, $^{**}P < 0.01$ by two-way ANOVA with Tukey's multiple comparisons test, $n = 5$. (L) RT-qPCR analysis of the mRNA levels of neurotoxic markers in the Substantia nigra tissue. $^{*}P < 0.05$, $^{**}P < 0.01$ by two-way ANOVA with Tukey's multiple comparisons test, $n = 5$. (M, N) Representative immunoblots and quantification of C3, TH, PCNA, GFAP, FGF7, and β-Arrestin2 in the substantia nigra tissue. $^{*}P < 0.05$ by two-way ANOVA with Tukey's multiple comparisons test, $n = 5$.

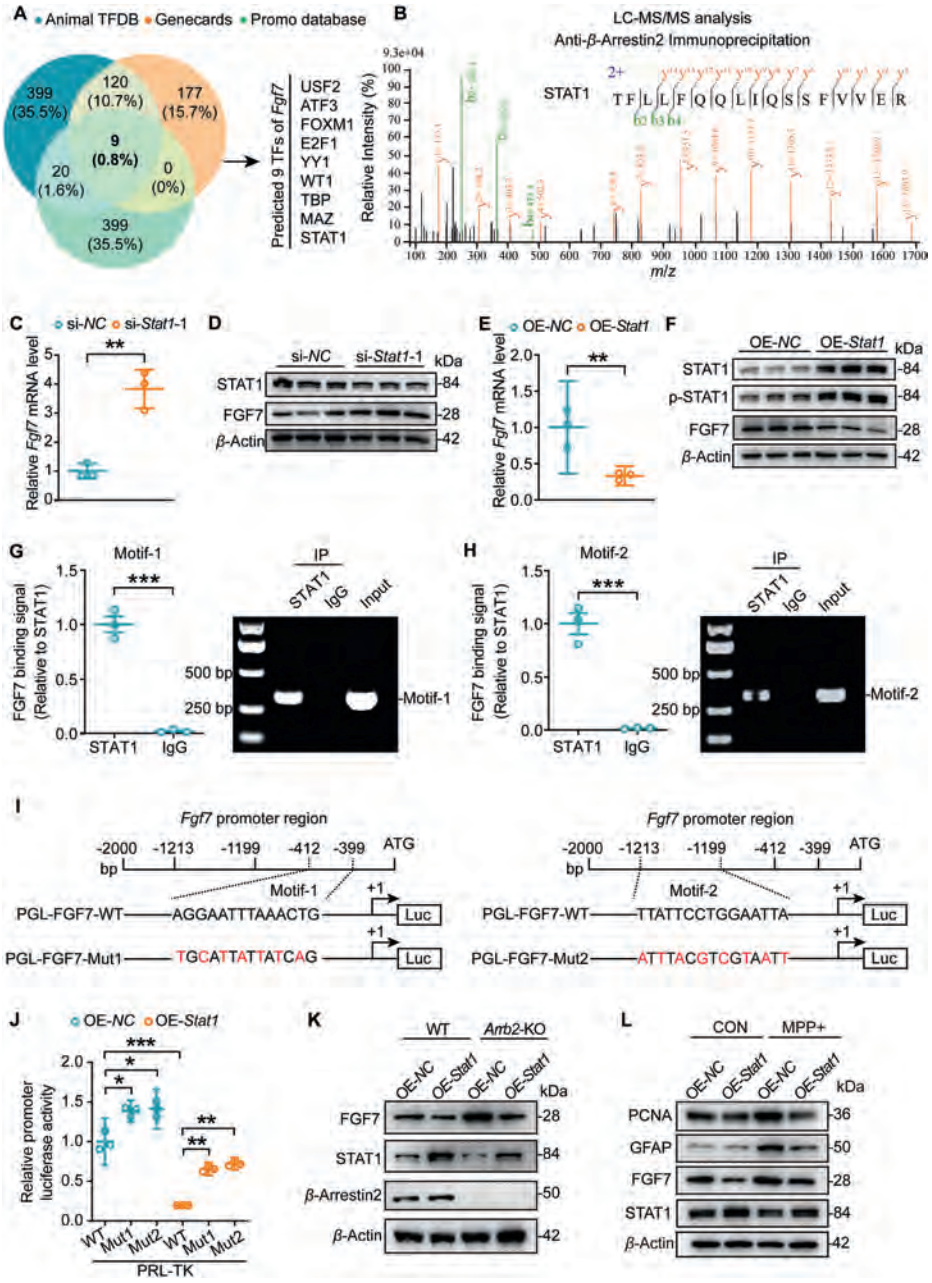

Figure 6 STAT1 is a transcription factor suppressing *Fgf7* expression in the presence of β-Arrestin2. (A) Venn diagram displaying the number of transcription factors of *Fgf7* predicted by Animal TFDB, Genecards and Promo database. The 9 overlapped transcription factors are displayed in the right panel. (B) Anti-β-Arrestin2 immunoprecipitation showing STAT1 as the transcription factor of *Fgf7* in astrocytes analyzed by LC−MS/MS. (C) RT-qPCR analysis of *Fgf7* mRNA level in *Stat1* knockdown astrocytes. $^{**}P < 0.01$ by unpaired *t* test, $n = 3$. (D) Representative immunoblots of STAT1 and FGF7 showing the effect of *Stat1* knockdown on FGF7 expression in astrocytes. (E) RT-qPCR analysis of *Fgf7* mRNA level in *Stat1* overexpression astrocytes. $^{**}P < 0.01$ by unpaired *t* test, $n = 3$. (F) Representative immunoblots of p-STAT1/STAT1 and FGF7 showing the effect of *Stat1* overexpression on FGF7 expression in astrocytes. (G, H) ChIP-qPCR and PCR analyses of *Fgf7* binding signal from anti-IgG and anti-STAT1 immunoprecipitation in astrocytes. $^{***}P < 0.001$ by unpaired *t* test, $n = 3$. (I) Illustration showing WT and two mutant sequences of *Fgf7* motifs. (J) Luciferase reporter assay showing the effect of *Stat1* overexpression on *Fgf7* promoter activity in HEK293T cells. $^{*}P < 0.05$, $^{**}P < 0.01$, $^{***}P < 0.001$ by one-way ANOVA with Tukey's multiple comparisons test, $n = 3$. (K) Representative immunoblots of FGF7, STAT1 and β-Arrestin2 in WT and *Arrb2* KO astrocytes with *Stat1* overexpression. (L) Representative immunoblots of PCNA, GFAP, FGF7, and STAT1 in *Stat1* overexpression astrocytes with MPP $^{+}$ treatment.

the reduction in FGF7 production is mediated by Drd2/β-Arrestin2-biased signaling rather than Drd2/G protein-biased signaling. A previous study reported that microglial β-Arrestin1 and β-Arrestin2 were reciprocally regulated in PD context[35]. Consistently, our results showed that MPTP/MPP $^{+}$ treatment resulted in upregulated β-Arrestin1 and downregulated β-Arrestin2 expression in both astrocytes and microglia (Fig. S12F−S12H). However, *Arrb1* KO did not affect FGF7

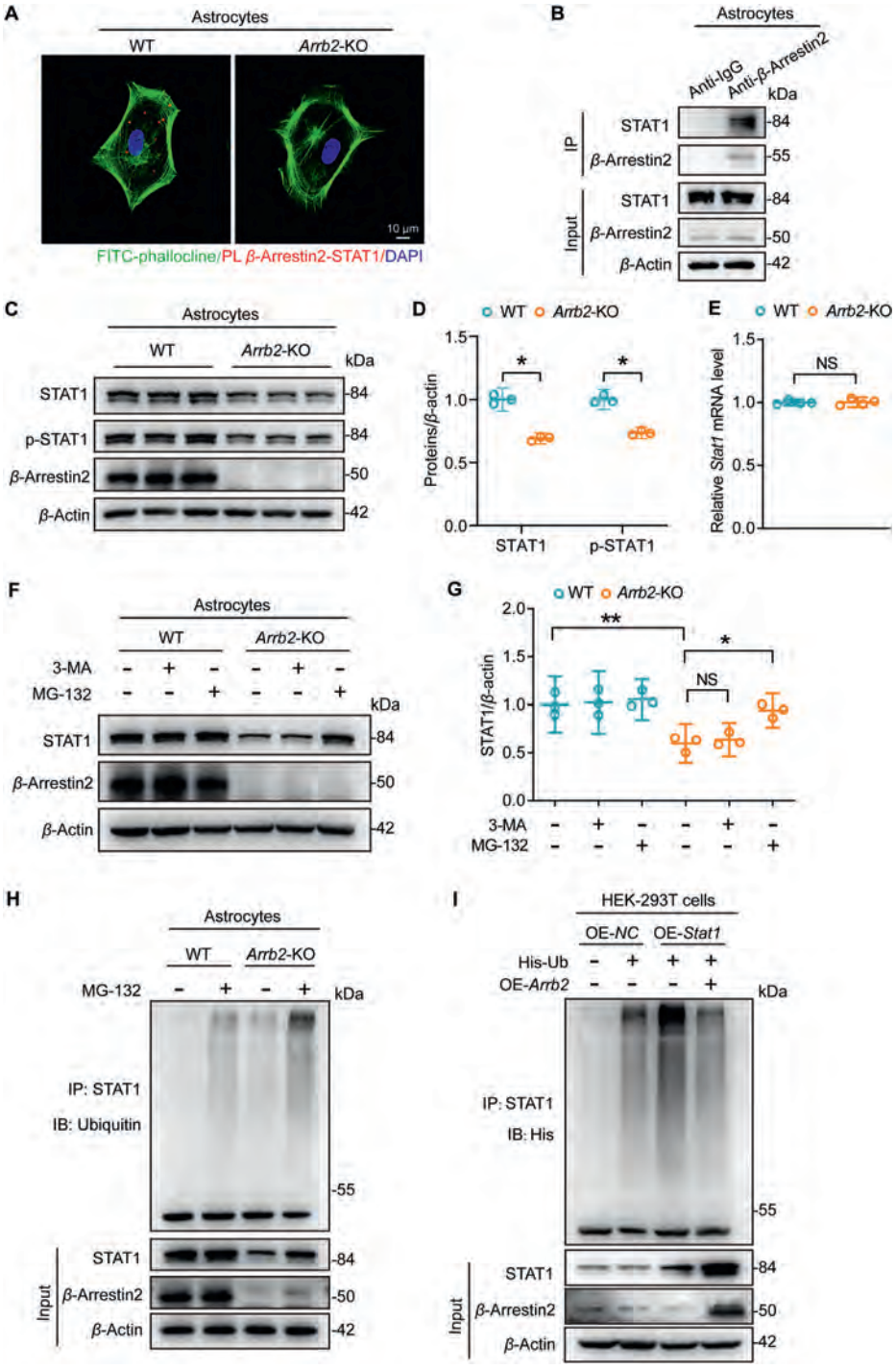

Figure 7 β-Arrestin2 deficiency boosts STAT1 degradation through ubiquitin-proteasomal pathway. (A) Proximity ligation assay showing the interaction between β-Arrestin2 and STAT1 (red dots) in WT and *Arrb2* KO astrocytes. Scale bar: 10 μm. (B) Co-immunoprecipitation experiments showing the interaction between β-Arrestin2 and STAT1 in astrocytes. (C, D) Representative immunoblots and quantification of p-STAT1/STAT1 and β-Arrestin2 in WT and *Arrb2* KO astrocytes. $^{*}P < 0.05$ by unpaired *t* test, $n = 3$. (E) RT-qPCR analysis of *Stat1* mRNA level in WT and *Arrb2* KO astrocytes. NS, no significance by unpaired *t* test, $n = 4$. (F, G) Representative immunoblots and quantification of STAT1 and β-Arrestin2 in WT and *Arrb2* KO astrocytes treated with 3-MA (5 mmol/L, 6 h) or MG132 (10 mmol/L, 6 h). $^{*}P < 0.05$, $^{**}P < 0.01$ by two-way ANOVA with Tukey's multiple comparisons test. NS, no significance, $n = 3$. (H) Representative immunoblots of Ubiquitin, STAT1 and β-Arrestin2 in WT and *Arrb2* KO astrocytes treated with or without MG132 (10 mmol/L, 6 h). (I) Representative immunoblots of His, STAT1, and β-Arrestin2 in HEK-293T cells transfected with *Stat1*, Ubiquitin and *Arrb2* plasmids.

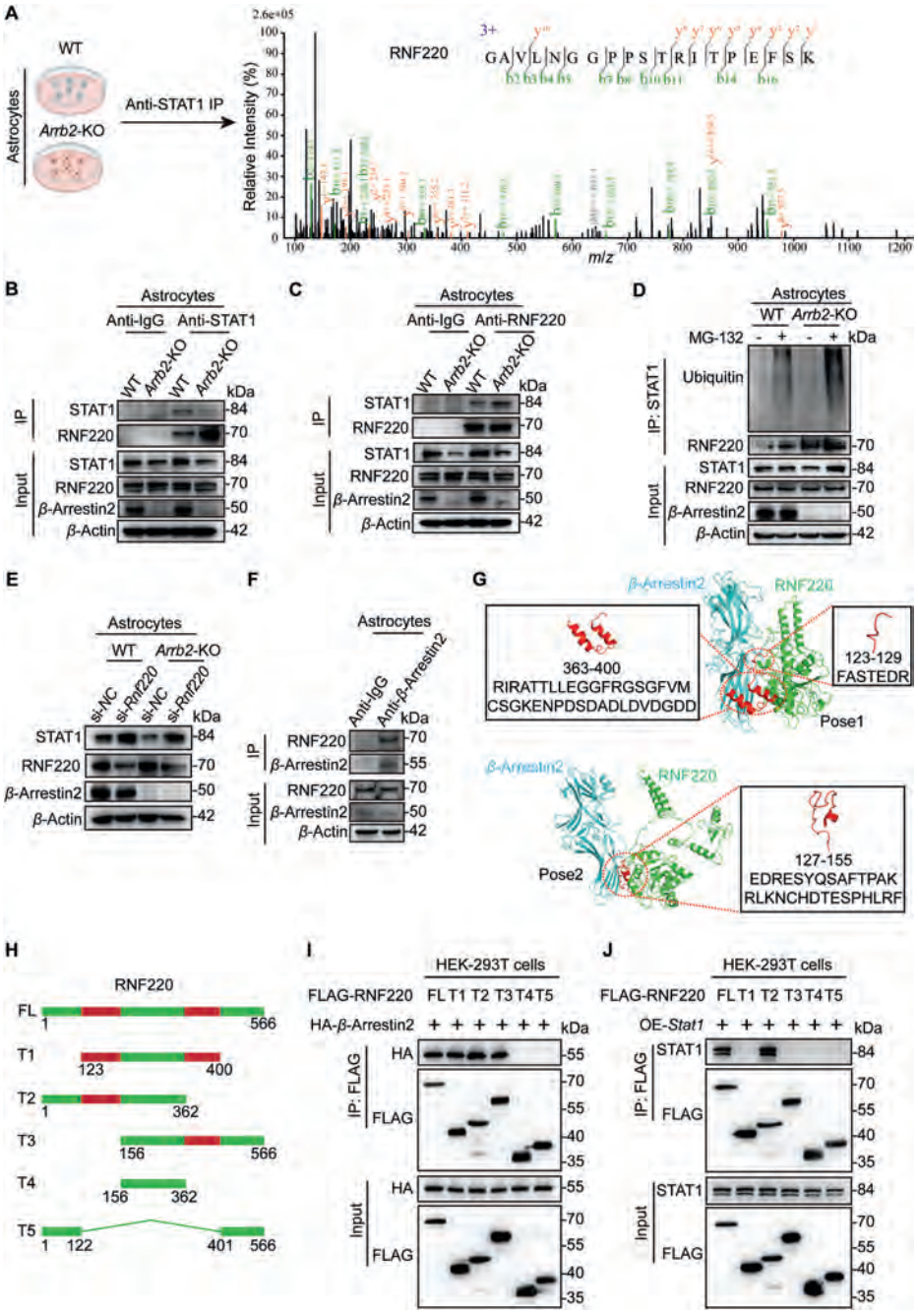

Figure 8 Inhibition of STAT1 degradation is facilitated by the binding of β-Arrestin2 to RNF220. (A) Anti-STAT1 immunoprecipitation from WT and *Arrb2* KO astrocytes showing RNF220 as an E3 ubiquitin ligase for STAT1 analyzed by LC−MS/MS. (B, C) Co-immunoprecipitation experiments showing the interaction between STAT1 and RNF220 in astrocytes from anti-STAT1 immunoprecipitation and anti-RNF220 immunoprecipitation. (D) Representative immunoblots of Ubiquitin, RNF220, STAT1 and β-Arrestin2 in WT and *Arrb2* KO astrocytes treated with or without MG132. (E) Representative immunoblots of STAT1, RNF220 and β-Arrestin2 showing the effect of *Rnf220* knockdown on the expression of STAT1 in WT and *Arrb2* KO astrocytes. (F) Co-immunoprecipitation experiments showing the interaction between β-Arrestin2 and RNF220 in astrocytes from anti-β-Arrestin2 immunoprecipitation. (G) Illustration of the binding poses and sequences of β-Arrestin2 and RNF220 simulated by the ZDOCK module. (H) Construction of plasmids encoding full length (FL) and truncated forms (T1−T5) of RNF220. (I) Representative immunoblots of HA and FLAG showing the interaction between β-Arrestin2 and different forms of RNF220 in HEK-293T cells. (J) Representative immunoblots of STAT1 and FLAG showing the interaction between STAT1 and different forms of RNF220 in HEK-293T cells.

production in astrocytes (Fig. S12I). These results suggest that β-Arrestin2 specifically modulates FGF7-mediated neuroinflammation in astrocytes.

To establish the essential role of β-Arrestin2 in UNC9995-mediated inhibition of astrocyte reactivity, we examined the effect of UNC9995 treatment in *Arrb2* KO astrocytes. Our results showed that *Arrb2* KO blocked the inhibitory effect of UNC9995 on the elevated expression and production of FGF7 in MPP^+-treated astrocytes (Fig. 9A and B, Supporting Information Fig. S13A and S13B). Meanwhile, the inhibitory effects of

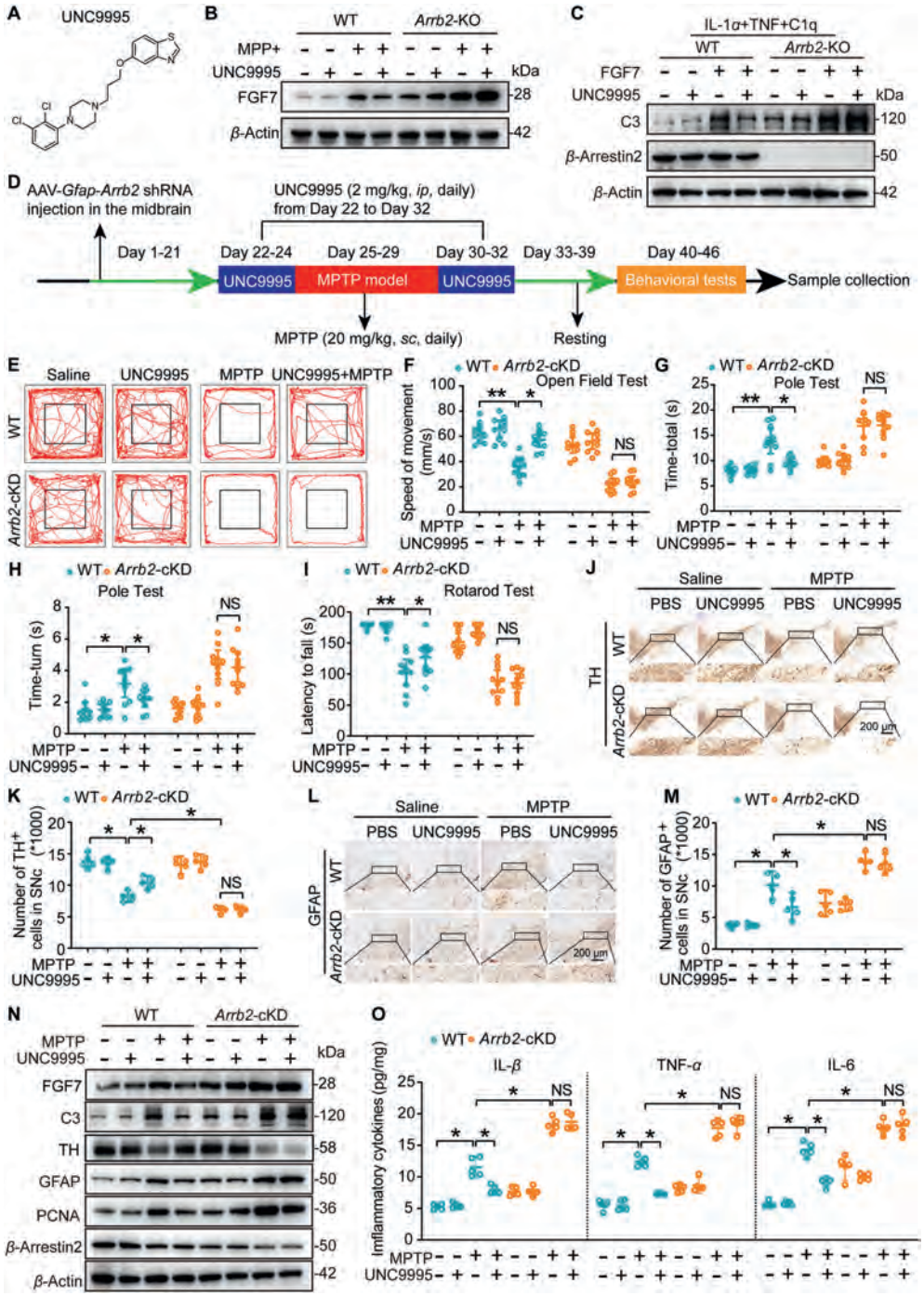

Figure 9 UNC9995 has therapeutic potential for MPTP-induced pathology through activation of Drd2/β-Arrestin2-biased signaling to reduce FGF7 production and reactive astrocytes. (A) Chemical structure of UNC9995. (B) Representative immunoblot showing the effect of UNC9995 (10 μmol/L, 1 h) pretreatment on FGF7 protein level in WT and *Arrb2* KO astrocytes exposed to MPP^+ (500 μmol/L, 24 h). (C) Representative immunoblot showing the effect of UNC9995 (10 μmol/L, 1 h) pretreatment on C3 protein level in WT and *Arrb2* KO astrocytes exposed to FGF7 (20 mg/mL, 24 h) in neurotoxic astrocyte model. (D) Experimental design to evaluate the therapeutic potential of UNC9995 on MPTP-induced pathology in WT and *Arrb2* cKD mice. (E, F) Representative travel paths (red) and quantification of the movement speed in the open field test. $^*P < 0.05$, $^{**}P < 0.01$ by two-way ANOVA with Tukey's multiple comparisons test. NS, no significance, $n = 10$. (G, H) Quantification of the total time and turn-around time spent in the pole test. $^*P < 0.05$, $^{**}P < 0.01$ by two-way ANOVA with Tukey's multiple comparisons test. NS, no significance, $n = 10$. (I) Quantification of the latency to fall in the rotarod test. $^*P < 0.05$, $^{**}P < 0.01$ by two-way ANOVA with Tukey's multiple comparisons test. NS, no significance, $n = 10$. (J, K) Representative images and quantification of TH immunostaining in the SNc region. Scale bar: 200 μm $^*P < 0.05$ by two-way ANOVA with Tukey's multiple comparisons test. NS, no significance, $n = 5$. (L, M) Representative images and quantification of GFAP immunostaining in the SNc region. Scale bar: 200 μm $^*P < 0.05$ by two-way ANOVA with Tukey's multiple comparisons test. NS, no significance, $n = 5$. (N) Representative immunoblot of FGF7, C3, TH, GFAP, PCNA, and β-Arrestin2 in the substantia nigra tissue. (O) ELISA assay showing the effect of UNC9995 treatment on inflammatory cytokines release in the Substantia nigra tissue. $^*P < 0.05$ by two-way ANOVA with Tukey's multiple comparisons test. NS, no significance, $n = 5$.

UNC9995 on astrocyte proliferation and reactivity in the presence of MPP^+ were impeded upon *Arrb2* KO (Fig. S13C−S13E). More importantly, in the neurotoxic astrocyte model, UNC9995 treatment restrained FGF7-stimulated upregulation of C3, but this effect was abolished upon *Arrb2* KO (Fig. 9C and Fig. S13F). These results indicate the potential of UNC9995 treatment in mitigating astrocyte reactivity and neurotoxicity, with β-Arrestin2 being a key participant.

Next, we proceeded to evaluate the therapeutic potential of UNC9995 in the MPTP mouse model. The AAV-*Gfap-Arrb2* shRNA was injected into the Substantia nigra for three weeks to generate *Arrb2* cKD mice. UNC9995 treatment was initiated three days prior to the MPTP model and continued until three days after the conclusion of the MPTP model. Subsequently, behavioral tests were conducted to evaluate the effects of UNC9995 (Fig. 9D). In the open field test, UNC9995 treatment increased the movement speed of MPTP-exposed WT mice, but not in *Arrb2* cKD mice (Fig. 9E and F). In the pole test, UNC9995 treatment reduced the total and turn-around time spent by WT but not *Arrb2* cKD mice treated with MPTP (Fig. 9G and H). In the rotarod test, MPTP-subjected mice exhibited reduced latency to fall, but UNC9995 treatment increased the latency to fall in WT mice, but not in *Arrb2* cKD mice (Fig. 9I). Most importantly, UNC9995 treatment attenuated the MPTP-induced loss of DA neurons in WT mice, but not in *Arrb2* cKD mice (Fig. 9J and K). UNC9995 treatment also reduced the increased astrocyte reactivity observed in MPTP-treated WT mice, but not in *Arrb2* cKD mice (Fig. 9L and M). Subsequently, we identified that the loss of astrocytic β-Arrestin2 blocked the inhibitory effect of UNC9995 on FGF7 expression (Fig. 9N and Fig. S13G). Consequently, the inhibition of astrocyte reactivity and the rescue of DA neurons by UNC9995 treatment was abolished in *Arrb2* cKD mice exposed to MPTP (Fig. 9N and Fig. S13H−S13L). Meanwhile, the effect of UNC9995 on the suppression of the release of proinflammatory cytokines by reactive astrocytes was blocked in *Arrb2* cKD mice exposed to MPTP (Fig. 9O). We further validated the neuroprotective effect of UNC9995 treatment in the LPS-induced PD model. Consistent with the MPTP results, activation of β-Arrestin2 using UNC9995 reduced GFAP-positive astrocytes, decreased FGF7 and proinflammatory cytokine levels, and protected against dopaminergic neuron loss in the LPS model (Supporting Information Fig. S14A−S14F). In summary, our results show that UNC9995 treatment activates the Drd2/β-Arrestin2 signaling pathway, leading to a reduction in FGF7 production in astrocytes and preventing the upregulated astrocyte reactivity.

4. Discussion

Astrocyte reactivity is increased intensively in PD[13], while the key variables shaping astrocyte reactivity are elusive. We previously observed a notable decrease in β-Arrestin2 level in MPTP-treated mice, while activating β-Arrestin2 mitigated inflammation-related neurodegeneration[28]. In this study, we have, for the first time, identified FGF7 as a molecular switch and β-Arrestin2 as a critical molecular brake on reactive astrocyte transformation in the PD context.

We show that β-Arrestin2, a multifunctional regulator of GPCR signaling, acts as a molecular brake on neurotoxic astrocyte reactivity. We employed the well-established neurotoxic astrocyte conversion model[5] to examine the role of *Arrb2* in regulating astrocyte reactivity. The reactive genes that responded to si-*Arrb2* in cultured astrocytes were found to be in agreement with prior reports[5]. However, we observed that only four genes from the established set of reactive genes, specifically *C3*, *Ligp1*, *Psmb8*, and *Amigo2*, exhibit a response to the *Arrb2* cKD/MPTP condition *in vivo*. This indicates the presence of a distinct subpopulation of neurotoxic reactive astrocytes in the *Arrb2* cKD/MPTP context, that may contribute to dopaminergic neuronal loss. Intriguingly, we observed that *Arrb2* KO astrocytes exhibited an increase in proliferation, and this proliferative capacity was further amplified in *Arrb2* KO astrocytes treated with MPP^+. This observed increase in the proliferation of *Arrb2* KO/MPP^+-induced reactive astrocytes distinguishes our findings from the non-proliferative nature of neurotoxic astrocytes reported previously[5]. Together, these findings establish β-Arrestin2 as a critical negative regulator of neurotoxic astrocyte reactivity and provide a potential therapeutic target to curb neuroinflammation and dopaminergic neurodegeneration in PD.

Unlike most members of the FGF family, we found that FGF7 is detrimental for the survival of DA neurons. Loss of β-Arrestin2 by MPTP/MPP^+ induction upregulates both mRNA and protein levels of FGF7, priming astrocytes towards a neurotoxic phenotype. However, knockdown of *Fgf7* attenuated neurotoxic phenotype transformation of *Arrb2* KO astrocytes. Therefore, we speculate that β-Arrestin2 serves as an upstream molecule that regulates FGF7 production to balance astrocyte reactivity. To testify, we generated astrocytic *Fgf7*/*Fgfr2* knockdown mice, and found that these mice were less susceptible to MPTP-induced pathology than WT mice. Notably, knockdown of astrocytic *Fgf7* restrained neurotoxic astrocyte reactivity in *Arrb2* KO mice. Therefore, we demonstrate that β-Arrestin2 maintains astrocyte homeostasis through the FGF7/FGFR2 signaling cascade in the MPTP condition. Intriguingly, we observed additive effects on FGF7 expression in astrocytes under *Arrb2* KO and MPP^+ conditions, which may be attributed to the multifaceted effects of MPP^+ treatment on multiple pathways[41,42]. Likewise, FGF7 treatment and IL-1α+TNF + C1q treatment also showed additive effects on astrocyte reactivity. The differences and interactions among the NF-κB pathway, IL-1 signaling, TNF signaling, and complement activation may account for the additive effects observed in astrocyte reactivity[43-45]. Given the established role of elevated FGF7 expression in potentiating astrocyte-driven neuroinflammatory cascades, a conserved pathogenic mechanism observed across multiple PD experimental paradigms, targeted suppression of FGF7 signaling may represent a viable therapeutic strategy to attenuate behavioral impairments and neuropathological hallmarks in alternative PD models, including those driven by α-synuclein mutations.

Phosphorylated STAT1 is primarily known as a transcriptional activator of genes, especially those stimulated by interferons[46,47]. However, several studies have also highlighted STAT1's role as a transcriptional repressor, where it negatively regulates the expression of certain genes such as *Sox9* and *Perlecan*[48,49]. In our study, we report that *FGF7* is a novel gene suppressed by STAT1. We further observed that lacking β-Arrestin2 enhanced proteasomal degradation of STAT1, resulting in overproduction of FGF7 in astrocytes. RNF220 was reported as the E3 ubiquitin ligase for STAT1 degradation, and the domain containing 1−314 aa of RNF220 was required for STAT1 binding[38]. Our data confirmed the binding of RNF220 to STAT1. Moreover, we identified that β-Arrestin2 blocks the binding between RNF220 and STAT1 *via* direct binding site occupation or steric hindrance. Together, we propose that loss of β-Arrestin2 in permits RNF220-mediated proteasomal degradation of STAT1, driving overexpression of FGF7 and activation of the FGF7/FGFR2 signaling axis. This

mechanism underlies the conversion of astrocytes to the neurotoxic phenotype (Supporting Information Fig. S15).

Biased agonists selective for G protein or β-Arrestin pathways offer an opportunity to develop therapeutic agents with reduced side effects[50,51]. Here, we report that activating Drd2/β-Arrestin2-biased signaling using UNC9995 reduces FGF7 production and prevents conversion of neurotoxic astrocytes, offering therapeutic effects for MPTP-exposed mice. Notably, neither G protein- nor β-Arrestin1-biased signaling impacted FGF7-driven neurotoxic astrocyte reactivity. Although β-Arrestin2-mediated signaling differs from the pathways activated in the IL-1α+TNF + C1q model, both conditions share common neurotoxic markers such as C3. To this end, we utilized the well-established IL-1α+TNF + C1q-induced neurotoxic astrocyte model to validate the inhibitory effect of UNC9995 on neurotoxic astrocyte conversion. Our data demonstrated that selectively activating the Drd2/β-Arrestin2 pathway with UNC9995 effectively maintained astrocyte homeostasis, suggesting β-Arrestin2-biased agonists as a promising strategy for managing astrocyte reactivity in PD.

5. Conclusions

In summary, our work reveals Drd2/β-Arrestin2 signaling as an upstream regulator of FGF7/FGFR2 autocrine signaling in astrocytes, demonstrating that astrocyte reactivity is governed by the interplay between these two pathways. Importantly, β-Arrestin2-biased agonists may enhance its protective role, while inhibitors of FGF7/FGFR2 signaling could mitigate neurotoxic astrocyte reactivity. Given that dysregulated astrocyte activity is a common pathological feature across multiple neurodegenerative diseases, targeting these signaling may hold broader therapeutic potential beyond PD. Further work is still needed to fully elucidate how FGF7 impacts DA neuronal survival. Nevertheless, this study provides mechanistic insight into astrocyte phenotypes in the context of MPTP/MPP^+, and pave the way for developing disease-modifying treatments aimed at reactive astrocytes.

Acknowledgements

This work was supported by grants from the National Key R&D Program of China (No. 2021ZD0202903), the National Natural Science Foundation of China (Nos. 82373851, 82173797, and 82204357) and the Natural Science Foundation of Jiangsu Province (BK20231267, China).

Author contributions

Ming Lu and Lei Cao conceived this project. Xin Sun performed most experiments and analyzed the data. Yueping Wang performed AAVs injection and behavioral tests. Yajie Zhang performed the RNA sequencing experiments and bioinformatics analysis. Ruixue Han and Min Wang assisted in data collection and visualization. Jing Zhang, Ting Sun and Yang Liu did the cell culture and bioinformatics analysis. Lei Cao wrote the manuscript with input from all authors. Ming Lu and Gang Hu supervised the project and revised the manuscript. Ming Lu and Lei Cao acquired funds.

Conflicts of interest

The authors declare no competing interests.

Appendix A. Supporting information

Supporting information to this article can be found online at https://doi.org/10.1016/j.apsb.2025.07.012.

References

1. Obeso JA, Stamelou M, Goetz CG, Poewe W, Lang AE, Weintraub D, et al. Past, present, and future of Parkinson's disease: a special essay on the 200th Anniversary of the Shaking Palsy. *Mov Disord* 2017;**32**:1264−310.
2. Tunik E, Feldman AG, Poizner H. Dopamine replacement therapy does not restore the ability of Parkinsonian patients to make rapid adjustments in motor strategies according to changing sensorimotor contexts. *Parkinsonism Relat Disord* 2007;**13**:425−33.
3. Paul SS, Schaefer SY, Olivier GN, Walter CS, Lohse KR, Dibble LE. Dopamine replacement medication does not influence implicit learning of a stepping task in people with Parkinson's disease. *Neurorehabil Neural Repair* 2018;**32**:1031−42.
4. Vijiaratnam N, Simuni T, Bandmann O, Morris HR, Foltynie T. Progress towards therapies for disease modification in Parkinson's disease. *Lancet Neurol* 2021;**20**:559−72.
5. Liddelow SA, Guttenplan KA, Clarke LE, Bennett FC, Bohlen CJ, Schirmer L, et al. Neurotoxic reactive astrocytes are induced by activated microglia. *Nature* 2017;**541**:481−7.
6. Zhang L, Jia Z, Wu Q, Bai T, Wang B, Hu X, et al. Alleviating symptoms of neurodegenerative disorders by astrocyte-specific overexpression of TMEM164 in mice. *Nat Metab* 2023;**5**:1787−802.
7. Cameron EG, Nahmou M, Toth AB, Heo L, Tanasa B, Dalal R, et al. A molecular switch for neuroprotective astrocyte reactivity. *Nature* 2024;**626**:574−82.
8. Patani R, Hardingham GE, Liddelow SA. Functional roles of reactive astrocytes in neuroinflammation and neurodegeneration. *Nat Rev Neurol* 2023;**19**:395−409.
9. Hasel P, Rose IVL, Sadick JS, Kim RD, Liddelow SA. Neuroinflammatory astrocyte subtypes in the mouse brain. *Nat Neurosci* 2021;**24**:1475−87.
10. Smajic S, Prada-Medina CA, Landoulsi Z, Ghelfi J, Delcambre S, Dietrich C, et al. Single-cell sequencing of human midbrain reveals glial activation and a Parkinson-specific neuronal state. *Brain* 2022;**145**:964−78.
11. Chen ZP, Wang S, Zhao X, Fang W, Wang Z, Ye H, et al. Lipid-accumulated reactive astrocytes promote disease progression in epilepsy. *Nat Neurosci* 2023;**26**:542−54.
12. Barbar L, Jain T, Zimmer M, Kruglikov I, Sadick JS, Wang M, et al. CD49f is a novel marker of functional and reactive human iPSC-derived astrocytes. *Neuron* 2020;**107**:436-53.e12.
13. Yun SP, Kam TI, Panicker N, Kim S, Oh Y, Park JS, et al. Block of A1 astrocyte conversion by microglia is neuroprotective in models of Parkinson's disease. *Nat Med* 2018;**24**:931−8.
14. Liu Y, Cao L, Song Y, Kang Z, Liu T, Ding J, et al. Mitochondrial glutamine transporter SLC1A5_var, a potential target to suppress astrocyte reactivity in Parkinson's disease. *Cell Death Dis* 2022;**13**:946.
15. Beenken A, Mohammadi M. The FGF family: biology, pathophysiology and therapy. *Nat Rev Drug Discov* 2009;**8**:235−53.
16. Xie Y, Su N, Yang J, Tan Q, Huang S, Jin M, et al. FGF/FGFR signaling in health and disease. *Signal Transduct Target Ther* 2020;**5**:181.
17. Liu Y, Deng J, Liu Y, Li W, Nie X. FGF, Mechanism of action, role in Parkinson's disease, and therapeutics. *Front Pharmacol* 2021;**12**:675725.
18. Zhang X, Pu X, Pi C, Xie J. The role of fibroblast growth factor 7 in cartilage development and diseases. *Life Sci* 2023;**326**:121804.
19. Tranchevent LC, Halder R, Glaab E. Systems level analysis of sex-dependent gene expression changes in Parkinson's disease. *npj Parkinson's Dis* 2023;**9**:8.

20. Dunckley T, Beach TG, Ramsey KE, Grover A, Mastroeni D, Walker DG, et al. Gene expression correlates of neurofibrillary tangles in Alzheimer's disease. *Neurobiol Aging* 2006;**27**:1359−71.
21. Morello G, La Cognata V, Guarnaccia M, La Bella V, Conforti FL, Cavallaro S. A diagnostic gene-expression signature in fibroblasts of amyotrophic lateral sclerosis. *Cells* 2023;**12**:1884.
22. Kang K, Lee SW, Han JE, Choi JW, Song MR. The complex morphology of reactive astrocytes controlled by fibroblast growth factor signaling. *Glia* 2014;**62**:1328−44.
23. Rajagopal S, Shenoy SK. GPCR desensitization: acute and prolonged phases. *Cell Signal* 2018;**41**:9−16.
24. Pandey S, Kumari P, Baidya M, Kise R, Cao Y, Dwivedi-Agnihotri H, et al. Intrinsic bias at non-canonical, β-arrestin-coupled seven transmembrane receptors. *Mol Cell* 2021;**81**:4605-21.e11.
25. Smith JS, Pack TF, Inoue A, Lee C, Zheng K, Choi I, et al. Noncanonical scaffolding of Gαi and β-arrestin by G protein-coupled receptors. *Science* 2021;**371**:eaay1833.
26. Qu C, Park JY, Yun MW, He QT, Yang F, Kim K, et al. Scaffolding mechanism of arrestin-2 in the cRaf/MEK1/ERK signaling cascade. *Proc Natl Acad Sci U S A* 2021;**118**:e2026491118.
27. Borroto-Escuela DO, Fuxe K. Diversity and bias through dopamine D2R heteroreceptor complexes. *Curr Opin Pharmacol* 2017;**32**:16−22.
28. Zhu J, Hu Z, Han X, Wang D, Jiang Q, Ding J, et al. Dopamine D2 receptor restricts astrocytic NLRP3 inflammasome activation *via* enhancing the interaction of β-arrestin2 and NLRP3. *Cell Death Differ* 2018;**25**:2037−49.
29. Du RH, Zhou Y, Xia ML, Lu M, Ding JH, Hu G. α-Synuclein disrupts the anti-inflammatory role of Drd2 *via* interfering β-arrestin2-TAB1 interaction in astrocytes. *J Neuroinflammation* 2018;**15**:258.
30. Zhang ZR, Zhang XR, Luan XQ, Wang XS, Wang WW, Wang XY, et al. Striatal overexpression of β-arrestin2 counteracts L-dopa-induced dyskinesia in 6-hydroxydopamine lesioned Parkinson's disease rats. *Neurochem Int* 2019;**131**:104543.
31. Longair MH, Baker DA, Armstrong JD. Simple Neurite Tracer: open source software for reconstruction, visualization and analysis of neuronal processes. *Bioinformatics* 2011;**27**:2453−4.
32. Ferreira TA, Blackman AV, Oyrer J, Jayabal S, Chung AJ, Watt AJ, et al. Neuronal morphometry directly from bitmap images. *Nat Methods* 2014;**11**:982−4.
33. Cao L, Xiong S, Wu Z, Ding L, Zhou Y, Sun H, et al. Anti-Na^+/K^+-ATPase immunotherapy ameliorates α-synuclein pathology through activation of Na^+/K^+-ATPase α1-dependent autophagy. *Sci Adv* 2021;**7**:eabc5062.
34. Wei Y, Lu M, Mei M, Wang H, Han Z, Chen M, et al. Pyridoxine induces glutathione synthesis *via* PKM2-mediated Nrf2 transactivation and confers neuroprotection. *Nat Commun* 2020;**11**:941.
35. Fang Y, Jiang Q, Li S, Zhu H, Xu R, Song N, et al. Opposing functions of β-arrestin 1 and 2 in Parkinson's disease *via* microglia inflammation and Nprl3. *Cell Death Differ* 2021;**28**:1822−36.
36. Pons-Espinal M, Blasco-Agell L, Fernandez-Carasa I, Andres-Benito P, di Domenico A, Richaud-Patin Y, et al. Blocking IL-6 signaling prevents astrocyte-induced neurodegeneration in an iPSC-based model of Parkinson's disease. *JCI Insight* 2024;**9**:e163359.
37. Dubey AR, Jagtap YA, Kumar P, Patwa SM, Kinger S, Kumar A, et al. Biochemical strategies of E3 ubiquitin ligases target viruses in critical diseases. *J Cell Biochem* 2022;**123**:161−82.
38. Guo X, Ma P, Li Y, Yang Y, Wang C, Xu T, et al. RNF220 mediates K63-linked polyubiquitination of STAT1 and promotes host defense. *Cell Death Differ* 2021;**28**:640−56.
39. Liu Y, Song N, Yao H, Jiang S, Wang Y, Zheng Y, et al. β-Arrestin2-biased Drd2 agonist UNC9995 alleviates astrocyte inflammatory injury *via* interaction between β-arrestin2 and STAT3 in mouse model of depression. *J Neuroinflammation* 2022;**19**:240.
40. Zhu J, Sun T, Zhang J, Liu Y, Wang D, Zhu H, et al. Drd2 biased agonist prevents neurodegeneration against NLRP3 inflammasome in Parkinson's disease model *via* a β-arrestin2-biased mechanism. *Brain Behav Immun* 2020;**90**:259−71.
41. Chen X, Liu Z, Cao BB, Qiu YH, Peng YP. TGF-β1 neuroprotection *via* inhibition of microglial activation in a rat model of Parkinson's disease. *J Neuroimmune Pharmacol* 2017;**12**:433−46.
42. Correll KA, Edeen KE, Redente EF, Zemans RL, Edelman BL, Danhorn T, et al. TGFβ inhibits HGF, FGF7, and FGF10 expression in normal and IPF lung fibroblasts. *Physiol Rep* 2018;**6**:e13794.
43. Pousset F, Dantzer R, Kelley KW, Parnet P. Interleukin-1 signaling in mouse astrocytes involves Akt: a study with interleukin-4 and IL-10. *Eur Cytokine Netw* 2000;**11**:427−34.
44. Kim H, Leng K, Park J, Sorets AG, Kim S, Shostak A, et al. Reactive astrocytes transduce inflammation in a blood−brain barrier model through a TNF−STAT3 signaling axis and secretion of α1-antichymotrypsin. *Nat Commun* 2022;**13**:6581.
45. Chen Y, Chu JM, Wong GT, Chang RC. Complement C3 from astrocytes plays significant roles in sustained activation of microglia and cognitive dysfunctions triggered by systemic inflammation after laparotomy in adult male mice. *J Neuroimmune Pharmacol* 2024;**19**:8.
46. Ren J, Li N, Pei S, Lian Y, Li L, Peng Y, et al. Histone methyltransferase WHSC1 loss dampens MHC-I antigen presentation pathway to impair IFN-γ-stimulated antitumor immunity. *J Clin Investig* 2022;**132**:e153167.
47. Zafar A, Pong Ng H, Diamond-Zaluski R, Kim GD, Ricky Chan E, Dunwoodie SL, et al. CITED2 inhibits STAT1−IRF1 signaling and atherogenesis. *FASEB J* 2021;**35**:e21833.
48. Imitola J, Hollingsworth EW, Watanabe F, Olah M, Elyaman W, Starossom S, et al. Stat1 is an inducible transcriptional repressor of neural stem cells self-renewal program during neuroinflammation. *Front Cell Neurosci* 2023;**17**:1156802.
49. Sharma B, Iozzo RV. Transcriptional silencing of perlecan gene expression by interferon-γ. *J Biol Chem* 1998;**273**:4642−6.
50. Hauser AS, Attwood MM, Rask-Andersen M, Schioth HB, Gloriam DE. Trends in GPCR drug discovery: new agents, targets and indications. *Nat Rev Drug Discov* 2017;**16**:829−42.
51. Kurose H, Kim SG. Pharmacology of antagonism of GPCR. *Biol Pharm Bull* 2022;**45**:669−74.